

<sup>1</sup>  
<sup>2</sup> Susceptible host dynamics explain pathogen resilience to  
<sup>3</sup> perturbations

<sup>4</sup>  
<sup>5</sup> Sang Woo Park, . . . , Sarah Cobey

<sup>6</sup> **Abstract**

<sup>7</sup> Major priority for epidemiological research in the time of anthropogenic change is  
<sup>8</sup> understanding how infectious disease dynamics respond to perturbations. Interven-  
<sup>9</sup> tions to slow the spread of SARS-CoV-2 significantly disrupted the transmission  
<sup>10</sup> of other human pathogens. As interventions lifted, whether and when respiratory  
<sup>11</sup> pathogens would eventually return to their pre-pandemic dynamics remains to be  
<sup>12</sup> answered. To address this gap, we develop a framework for estimating pathogen re-  
<sup>13</sup> silience based on how fast epidemic patterns return to their pre-pandemic, endemic  
<sup>14</sup> dynamics. Our analysis suggests that some pathogens may have settled to endemic  
<sup>15</sup> cycles that are different from their pre-pandemic patterns. Finally, we show that  
<sup>16</sup> the replenishment rate of the susceptible pool is a key determinant of pathogen re-  
<sup>17</sup> silience. Our framework offers a novel perspective to characterizing the dynamics of  
<sup>18</sup> endemic pathogens and their responses to SARS-CoV-2 interventions. [SWP: Need  
<sup>19</sup> to emphasize broader implications.]

Non-pharmaceutical interventions (NPIs) to slow the spread of SARS-CoV-2 disrupted the transmission of other human pathogens, providing large-scale natural experiments for understanding how various host-pathogen systems respond to perturbations [1, 2, 3, 4]. As interventions lifted, large heterogeneities in outbreak dynamics were observed across different pathogens in different countries (Figure 1), likely reflecting differences in NPI patterns, pathogen characteristics, immigration/importation from other countries, and pre-pandemic pathogen dynamics [5]. Understanding how different factors shape these re-emergence patterns has remained a key challenge for predicting future outbreaks, including whether we will see persistent changes in pathogen dynamics.

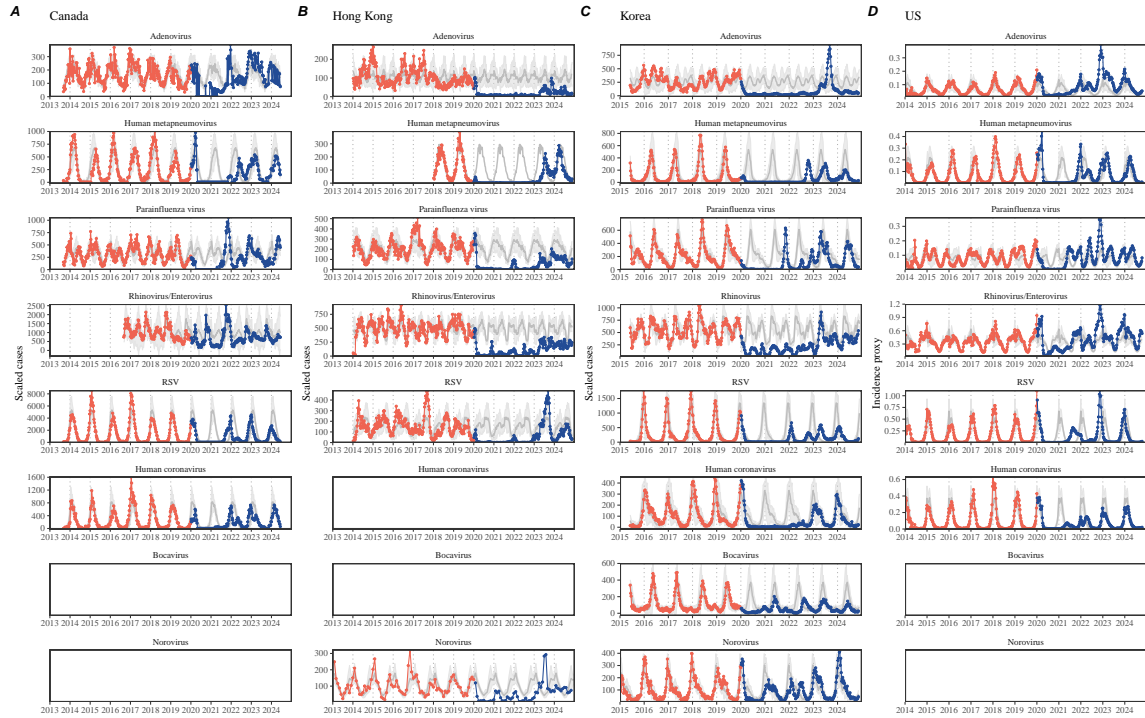


**Figure 1: Observed heterogeneity in responses to COVID-19 pandemic across respiratory pathogens and norovirus in (A) Canada, (B) Hong Kong, (C) Korea, and (D) US.** Red points and lines represent data before 2020. Blue points and lines represent data since 2020. Gray lines and shaded regions represent the mean seasonal patterns and corresponding 95% confidence intervals based on the observed outbreak patterns before 2020.

More than five years have passed since the emergence of SARS-CoV-2, and we now have potential evidence for persistent changes in pathogen dynamics following the pandemic, which likely reflect permanent shift in either human behavior or population-level immunity [6, 7]. For example, compared to pre-pandemic, seasonal patterns, human metapneumovirus and bocavirus in Korea are circulating at lower levels, whereas RSV in Korea seem to exhibit different seasonality (Figure 1). These

36 observations pose two fundamental questions for current and future infectious disease  
37 dynamics: (1) can we learn about underlying pathogen characteristics, such as their  
38 transmissibility or duration of immunity, from re-emergence patterns? and (2) can  
39 we predict whether and when other respiratory pathogens will eventually return to  
40 their pre-pandemic dynamics?

41 Understanding how ecological systems respond to perturbations is a fundamental  
42 challenge in predicting population persistence and extinction [8, 9, 10]. These re-  
43 sponds can be characterized in terms of resilience, which often measures how fast a  
44 system returns to its stable, reference state following a perturbation [11, 12, 13, 14].  
45 Theoretical and empirical efforts to quantify resilience of ecological systems have pro-  
46 vided key insights for understanding the dynamics of complex systems and linking  
47 these findings to actionable strategies for species conservation [15]. However, de-  
48 spite rich literature on ecological resilience, there have been limited applications to  
49 measuring the resilience of host-pathogen systems, especially for human pathogens.

50 To address this question, we propose a framework for characterizing the resilience  
51 of a host-pathogen system based on how fast the system recovers from perturbation.  
52 We begin by laying out a few representative scenarios that capture the potential im-  
53 pact of COVID-19 interventions on endemic pathogen dynamics and illustrating how  
54 resilience can be measured by comparing the pre- and post-pandemic dynamics of  
55 susceptible and infected hosts. In practice, information on susceptible hosts are often  
56 unavailable, and traditional methods for reconstructing the dynamics of susceptible  
57 hosts require long-term endemic time series [16, 17], which cannot be applied due  
58 to disruptions in epidemic patterns caused by COVID-19 interventions. Instead, we  
59 utilize Takens' embedding theorem to reconstruct empirical attractors from data and  
60 further measure the distance from this empirical attractor [18]. This reconstruction  
61 allows us to characterize the rate at which this distance decreases over time, which  
62 correspond to pathogen resilience. We apply this framework to analyzing pathogen  
63 surveillance data for a wide array of respiratory and non-respiratory pathogens from  
64 Canada, Hong Kong, Korea, and US. Finally, we show that susceptible host dynamics  
65 are a key determinants of pathogen resilience. Our study offers unique insights into  
66 understanding pathogen re-emergence patterns following COVID-19 interventions.

## 67 **Conceptual introduction to pathogen resilience**

68 In classical ecological literature, resilience of an ecological system is measured by  
69 the rate at which the system returns to its reference state following a perturbation  
70 [11, 12, 13, 14]. This rate corresponds to the largest real part of the eigenvalues of  
71 the linearized system near equilibrium—here, we refer to this value as the *intrinsic*  
72 resilience of the system, which represents the expected rate of return from perturbed  
73 states. However, respiratory pathogens often exhibit seasonal variation in transmis-  
74 sion, meaning that the intrinsic resilience of a host-pathogen system varies across  
75 season. Nonetheless, we can still measure the *empirical* resilience of a host-pathogen

76 system by looking at how fast the system returns to the pre-pandemic, endemic  
77 dynamics after interventions are lifted.

78 As an example, consider an intervention that reduce transmission by 50% for 6  
79 months starting in 2020, which causes epidemic patterns to deviate from its original  
80 stable annual cycle for a short period of time and eventually come back (Figure 2A).  
81 To measure the empirical resilience of this system, we first need to be able to measure  
82 the distance from its pre-pandemic attractor. There are many different ways we can  
83 measure the distance from attractor, but for illustrative purposes, we choose one of  
84 the most parsimonious approach: that is, we look at how the susceptible (S) and  
85 infected (I) populations change over time and measure the distance on the SI phase  
86 plane (Figure 2B). In this simple case, the locally estimated scatterplot smoothing  
87 (LOESS) fit indicates that the distance from attractor decreases linearly on average  
88 (Figure 2C). Furthermore, the overall rate of return matches the intrinsic resilience  
89 of the seasonally unforced system (Figure 2C).

90 Alternatively, NPIs can permanently change our behavior and have persisting  
91 impact on the pathogen dynamics; as an example, we consider a scenario in which a  
92 10% reduction in transmission persists even after the NPIs are lifted (Figure 2D–F).  
93 In such cases, we cannot know whether the pathogen will return to its original cycle  
94 or a different cycle until many years have passed after the NPIs are lifted, meaning  
95 that we cannot measure the distance against the new attractor that the system will  
96 eventually approach. Nonetheless, we can still measure the distance against the orig-  
97 inal, pre-pandemic attractor and ask how the distance changes over time (Figure 2E).  
98 The LOESS fit suggests that the distance from the attractor will initially decrease  
99 exponentially on average (equivalently, linearly on a log scale) and eventually plateau  
100 (Figure 2F). Here, a permanent 10% reduction in transmission rate slows down the  
101 system, which causes the distance from the attractor to decrease at a slower rate  
102 (Figure 2F) than it would have otherwise in the absence of permanent transmission  
103 reduction (Figure 2C). This example shows that resilience is not necessarily an in-  
104 trinsic property of a specific pathogen. Instead, pathogen resilience is a property of  
105 a specific attractor that a host-pathogen system approaches, which depends on both  
106 pathogen and host characteristics.

107 Finally, transient phenomena can also complicate the picture (Figure 2G–I). For  
108 example, a stage-structured model for RSV initially exhibits a stable annual cycle,  
109 but perturbations from NPIs cause the epidemic to exhibit biennial cycles (Figure  
110 2G). Despite this biennial cycle, we see that the system eventually approaches the  
111 original pre-pandemic attractor (Figure 2H), suggesting that this biennial cycle is a  
112 transient phenomenon. The LOESS fit indicates that the distance from the attractor  
113 will initially decrease exponentially at a rate that is consistent with the intrinsic  
114 resilience of the seasonally unforced system, but the rate of decrease slows down  
115 as the epidemic exhibits a biennial cycle (Figure 2I). In classical ecological theory,  
116 this behavior is also referred to as a ghost attractor, which causes long transient  
117 dynamics and slow transitions [19]. As we show in Supplementary Figure S1, strong  
118 seasonal forcing in transmission can also lead to transient phenomena for a simple

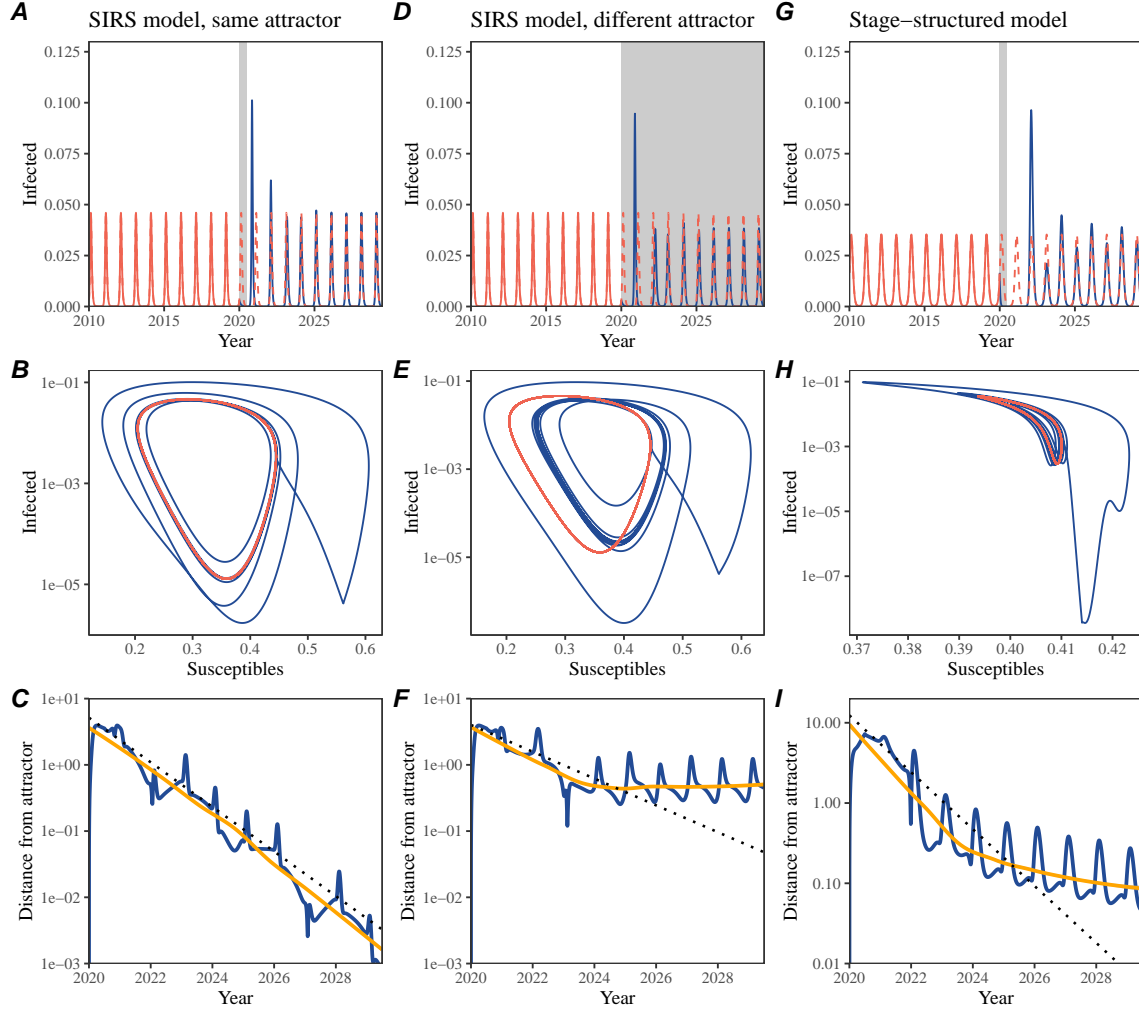


**Figure 2: Conceptual framework for measuring pathogen resilience following NPIs across different scenarios.** (A, D, G) Simulated epidemic trajectories across various models. Red and blue solid lines represent epidemic dynamics before and after interventions are introduced, respectively. Red dashed lines represent counterfactual epidemic dynamics in the absence of interventions. Gray regions indicate the duration of interventions. (B, E, H) Phase plane representation of the corresponding model. Red and blue solid lines represent epidemic trajectories on an SI phase plane before and after interventions are introduced, respectively. (C, F, I) Changes in logged distance from attractor over time. Blue lines represent the logged distance from attractor. Orange lines represent the locally estimated scatterplot smoothing (LOESS) fits to the logged distance from attractor. Dotted lines are superimposed as a comparison to have the same slope as the intrinsic resilience of the seasonally unforced system.

119 SIRS model, causing a slowing down of the system.

120 In Supplementary Materials, we also explore measuring the resilience of a two-  
121 strain host-pathogen system: when the dynamics two strains (or two pathogens) are  
122 coupled through cross immunity, we would expect the entire system to be character-  
123 ized by a single resilience value (rather than having two separate resilience for each  
124 strain). Simulations from a simple two-strain system illustrate that separate anal-  
125 yses of individual strain dynamics (e.g., RSV A vs B) and a joint analysis of total  
126 infections (e.g., total RSV infections) yield identical resilience estimates, confirming  
127 our expectation (Supplementary Figure S2, 3). Analogous to a single system, strong  
128 seasonal forcing in transmission can cause the system to slow down through transient  
129 phenomena (Supplementary Figure S4).

130 These observations indicate three possibilities. First, we can directly estimate  
131 the empirical resilience of a host-pathogen system by looking at how fast the system  
132 approaches a pre-pandemic attractor, provided that we can measure the distance  
133 from attractor. The empirical approach to estimating pathogen resilience is partic-  
134 ularly convenient because it does not require us to know the true underlying model.  
135 As we show in Supplementary Figure S5, estimating the intrinsic resilience from fit-  
136 ting standard compartmental models can lead to biased estimates, especially under  
137 model misspecification. Second, resilience estimates allow us to make phenomenolog-  
138 ical predictions about the dynamics of a host-pathogen system following a perturba-  
139 tion: assuming that the distance from the attractor will decrease exponentially over  
140 time, we can obtain a ballpark estimate for when the system will reach an attractor.  
141 Finally, deviation from an exponential decrease in the distance from attractor can  
142 provide information about whether the system has reached an alternative attractor,  
143 or a ghost attractor, that is different from the original, pre-pandemic attractor. These  
144 alternative attractors may reflect continued perturbations from permanent changes  
145 in transmission patterns as well as changes in immune landscapes.

## 146 **Inferring pathogen resilience from real data**

147 Based on these observations, we now set out to infer pathogen resilience from real  
148 data. Here, we briefly lay out our approach to estimating pathogen resilience from  
149 real data (Figure 3). We then test this approach against simulations and apply it to  
150 real data.

151 So far, we focused on simple examples that assume a constant transmission re-  
152 duction. However, in practice, the impact of NPIs on pathogen transmission is  
153 likely more complex (Figure 3A), reflecting introduction and relaxation of various  
154 intervention strategies. These complexities can lead to longer delays between the  
155 introduction of NPIs and pathogen re-emergence as well as temporal variation in  
156 outbreak sizes (Figure 3B): in this example, continued transmission reduction from  
157 NPIs limits the size of the first outbreak in 2021 following the emergence, allowing  
158 for a larger outbreak in 2022 when NPIs are further relaxed.

159 Previously, we relied on the dynamics of susceptible and infected hosts to compute

160 the distance from attractor (Figure 2), but information on susceptible hosts are  
161 often not available in practice. In addition, uncertainties in case counts due to  
162 observation error as well as the possibility of complex, multiannual attractor adds  
163 challenges to measuring the distance from attractor. To address these challenges, we  
164 first reconstruct an empirical attractor by utilizing Takens' theorem, which states  
165 that an attractor of a nonlinear multidimensional system can be mapped onto a  
166 delayed embedding [18]. Here, we use delayed copies of logged values of pre-pandemic  
167 cases  $C(t)$  (Figure 3C) to reconstruct the attractor:

$$\langle \log(C(t) + 1), \log(C(t - \tau) + 1), \dots, \log(C(t - (M - 1)\tau) + 1) \rangle, \quad (1)$$

168 where the delay  $\tau$  and embedding dimension  $M$  are determined based on autocor-  
169 relations and false nearest neighbors, respectively [20, 21]. We then apply the same  
170 delay and embedding dimensions to the entire time series to determine the position  
171 on a multi-dimensional state space (Figure 3D), which allows us to measure the  
172 nearest neighbor distance between the current state of the system and the empirical  
173 attractor (Figure 3E). In principle, we can quantify how fast this distance decreases  
174 by fitting a linear regression on a log scale, where the slope of the linear regression  
175 corresponds to pathogen resilience. As we show in Supplementary Figure S6, over-  
176 all temporal variations in the distance from attractor, especially the observed rate  
177 of decrease, appear robust to choices about embedding delays and dimensions; we  
178 note that using longer delays and higher dimensions tend to smooth out temporal  
179 variations in the distance from attractor.

180 Complex changes in the distance from attractor suggest that estimating pathogen  
181 resilience from linear regression will likely be sensitive to our choice of fitting windows  
182 for the regression. In Supplementary Materials, we explore an automated window  
183 selection criteria for linear regression and test it against randomized, stochastic sim-  
184 ulations across a wide range of realistic NPI shapes. We find that resilience estimates  
185 based on the automated window selection criteria are moderately correlated (0.48)  
186 with the intrinsic resilience of the post-NPI attractor (Supplementary Figure S7). In  
187 contrast, a naive approach that uses the entire time series, starting from the peak  
188 distance, only gives a correlation of 0.09 and consistently underestimates the intrinsic  
189 resilience (Supplementary Figure S7).

190 Now, we apply this approach to pathogen surveillance data presented in Figure  
191 1. For each time series, we apply Takens' theorem independently to reconstruct the  
192 empirical attractor and obtain the corresponding time series of distance from attrac-  
193 tors (Supplementary Figure S8 for the distance time series and linear regression fits).  
194 Then, we use the automated window selection criteria to fit a linear regression and  
195 estimate the empirical resilience for each pathogen in each country. For most res-  
196 piratory pathogens, resilience estimates fall between 0.4/year and 1.8/year (Figure  
197 4A), with the exception of Rhinovirus in the US (0.066/year; 95% CI: 0.018/year–  
198 0.113/year) and Bocavirus in Korea (0.087/year; 95% CI: 0.023/year–0.151/year).  
199 Excluding these exceptions, the mean resilience of common respiratory pathogens is  
200 0.974/year (95% CI: 0.784/year–1.16/year). As a reference, this is  $\approx 7$  times higher

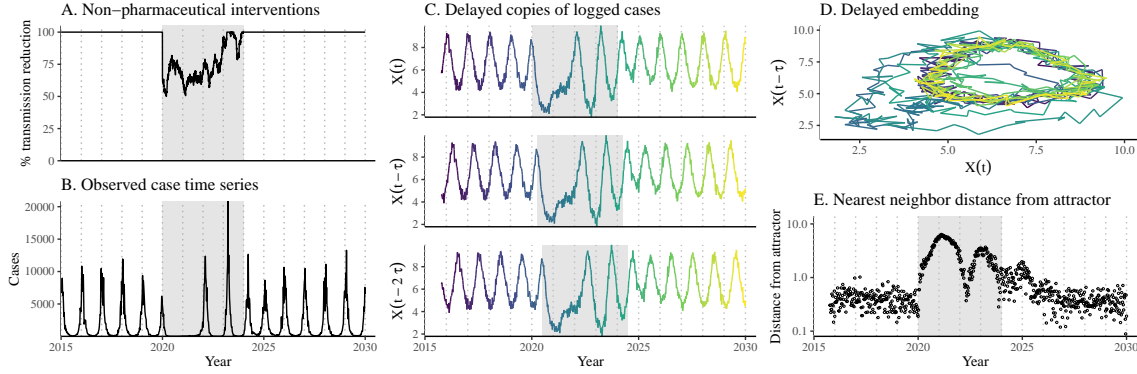


**Figure 3: A schematic diagram explaining how pathogen resilience can be inferred from real data.** (A) A realistic example of a synthetic NPI, represented by a relative reduction in transmission. (B) The impact of the synthetic NPI on epidemic dynamics simulated using a stochastic SIRS model. (C) Generating delayed copies of the logged time series allows us to obtain an embedding. (D) Two dimensional representation of an embedding. (E) Delayed embedding allows us to calculate the nearest neighbor distance from the empirical attractor, which is determined based on the pre-pandemic time series. This distance time series can be used to infer pathogen resilience by fitting a linear regression after choosing an appropriate window for regression.

than the intrinsic resilience of pre-vaccination measles dynamics ( $\approx 0.13/\text{year}$ ). Finally, resilience estimates for norovirus appears to be comparable to the intrinsic resilience of measles:  $0.119/\text{year}$  (95%CI:  $0.004/\text{year}$ – $0.233/\text{year}$ ) for Korea and  $0.385/\text{year}$  (95% CI:  $0.167/\text{year}$ – $0.603/\text{year}$ ). A simple ANOVA shows that there are significant differences in resilience estimates across countries ( $p < 0.036$ ) and pathogens ( $p < 0.030$ ).

Using resilience estimates, we now predict when each pathogen will return to their original pre-pandemic cycles. Specifically, we extend our linear regression fits to distance-from-attractor time series and ask when the predicted regression line will cross a threshold value, which we set to a mean of pre-pandemic distances. We predict that a return to pre-pandemic cycles would be imminent for most pathogens (Figure 4B; see Supplementary Figure S9 for a zoomed out version). In addition, we also predict that many pathogens should have already returned to their pre-pandemic dynamics by the end of 2024; but these predictions contradict some of the observed pathogen dynamics. For example, we predict that both human metapneumovirus and RSV in Korea should have returned to their attractors by now, but the magnitude and timing of recent epidemics are different from pre-pandemic patterns (Figure 1). These observations suggest the possibility that some common respiratory pathogens may have converged to different attractors.

In Supplementary Materials, we also consider using a lower threshold for the false nearest neighbor approach when determining the embedding dimension; this gives

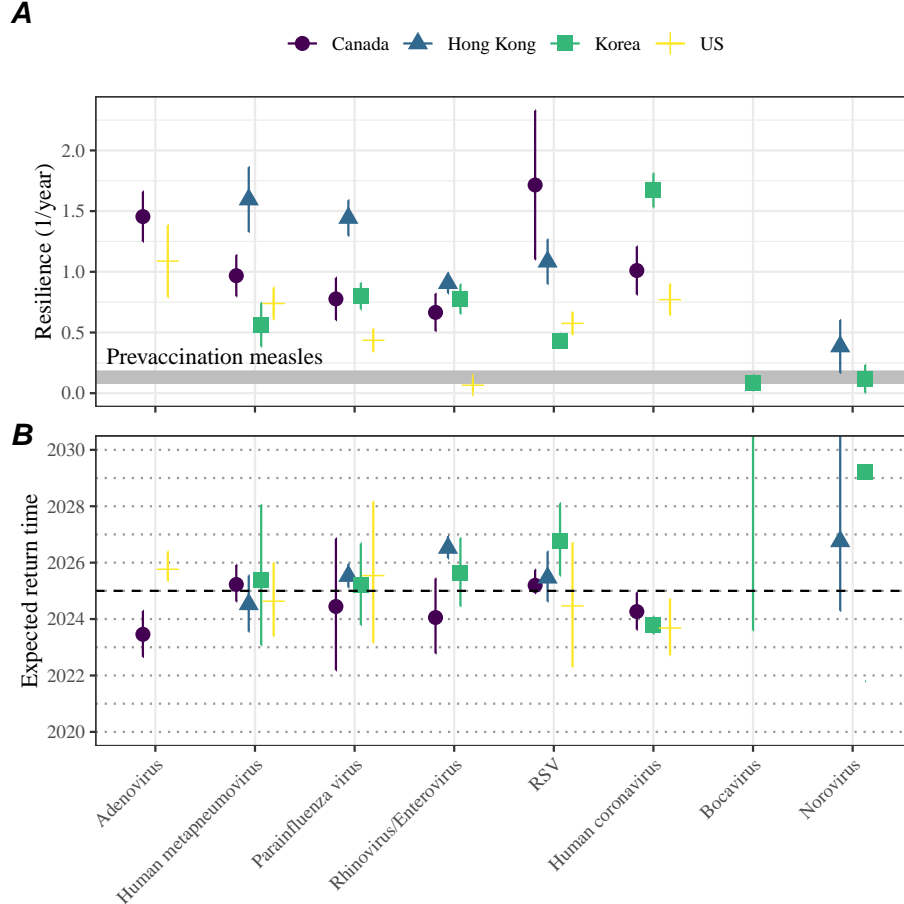


Figure 4: **Summary of resilience estimates.** (A) Estimated pathogen resilience. The gray horizontal line represents the intrinsic resilience of pre-vaccination measles dynamics. (B) Predicted timing of when each pathogen will return to their pre-pandemic cycles. The dashed line in panel B indicates the end of 2024 (current observation time). Error bars represent 95% confidence intervals.

a higher embedding dimension. As explained earlier (Supplementary Figure S6), this gives a smoother distance-from-attractor time series (compare Supplementary Figure S10 with S8); this also requires us to use longer time series, which prevents us from estimating resilience for some pathogens. Overall, resulting estimates of pathogen resilience with higher embedding dimensions still fall between 0.3/year and 2.1/year for the most part (Supplementary Figure S11). A direct comparison between two approaches (i.e., original estimate vs using higher dimensions) shows a strong consistency in resilience estimates (Supplementary Figure S12).

230 **Susceptible host dynamics explain variation in pathogen  
231 resilience**

232 So far, we focused on quantifying pathogen resilience from the observed patterns of  
 233 pathogen re-emergence following COVID-19 interventions. But what factors deter-  
 234 mine how resilient a host-pathogen system is? Here, we use a standard Susceptible-  
 235 Infected-Recovered-Susceptible (SIRS) model to show that susceptible host dynamics  
 236 are the key determinants of pathogen resilience. To do so, we vary the basic reproduc-  
 237 tion number  $\mathcal{R}_0$ , which represents the average number of secondary infections caused  
 238 by a newly infected individual in a fully susceptible population, and the duration of  
 239 immunity and compute intrinsic resilience for each parameter.

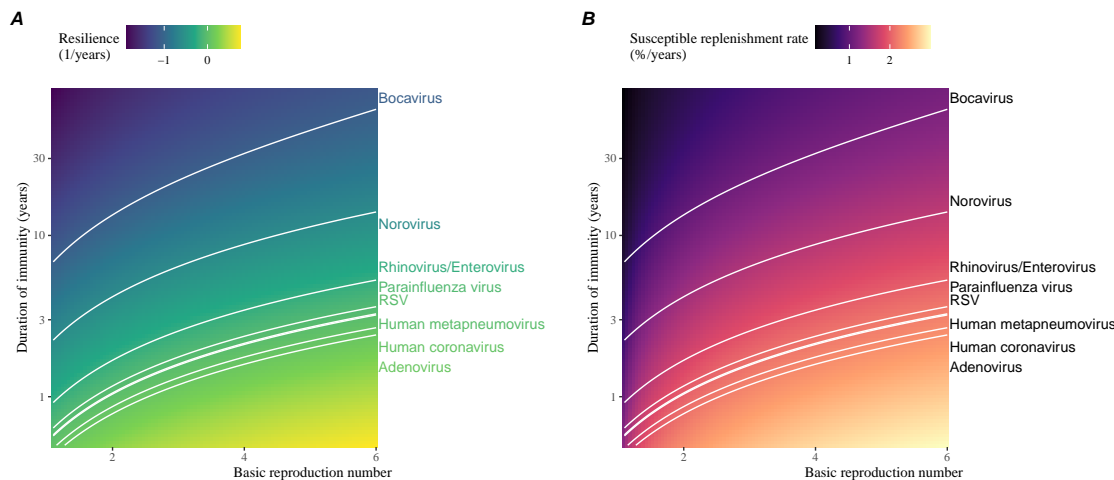


Figure 5: **Linking pathogen resilience to epidemiological parameters and susceptible host dynamics.** (A) The heat map represents intrinsic resilience as a function of the basic reproduction number  $\mathcal{R}_0$  and the duration of immunity. (B) The heat map represents per-capita susceptible replenishment rate as a function of the basic reproduction number  $\mathcal{R}_0$  and the duration of immunity. The standard SIRS model is used to compute intrinsic resilience and per-capita susceptible replenishment rate. Lines correspond to a set of parameters that are consistent with mean resilience estimates for each pathogen. Pathogens are ranked based on their mean resilience estimates, averaged across different countries.

240 We find an increase in  $\mathcal{R}_0$  and a decrease in duration of immunity correspond  
 241 to an increase in pathogen resilience (Figure 5A). These variations can be under-  
 242 stood in terms of the susceptible host dynamics, where faster per-capita susceptible  
 243 replenishment rate causes the system to be more resilient (Figure 5B). This rate can  
 244 be expressed as a ratio between absolute rate at which new susceptibles enter the  
 245 population and the equilibrium number of susceptible individuals in the population,  
 246  $\bar{S}$ . Therefore, both higher  $\mathcal{R}_0$  and shorter duration of immunity can drive faster

247 per-capita susceptible replenishment rate (Figure 5B), especially because higher  $\mathcal{R}_0$   
248 leads to lower  $\bar{S}$ .

249 Finally, we can now rank different pathogens based on the average values of em-  
250 pirical resilience, which allows us to determine a set of parameters that are consistent  
251 with the estimated resilience (Figure 5A). Across all pathogens we consider, except  
252 for bocavirus and norovirus, we estimate that the average duration of immunity is  
253 likely to be short (< 6 years) across a plausible range of  $\mathcal{R}_0$ . These rankings further  
254 allow us to map each pathogen onto a set of parameters that are consistent with  
255 its empirical resilience (Figure 5A) and obtain a plausible range of susceptible re-  
256 plenishment rates for each pathogen (Figure 5B). However, we note that there is no  
257 one-to-one correspondence between susceptible replenishment rates and pathogen re-  
258 silience, leading to a wide uncertainty in the estimates for susceptible replenishment  
259 rates (Figure 5B).

## 260 Discussion

261 The COVID-19 interventions have caused major disruptions to circulation patterns  
262 of both respiratory and non-respiratory pathogens, adding challenges to predicting  
263 their future dynamics [1, 2, 3, 4]. On the other hand, these interventions offer  
264 large-scale natural experiments for understanding how different pathogens respond to  
265 perturbations. In this study, we show that pathogen re-emergence patterns following  
266 COVID-19 interventions can be characterized through the lens of ecological resilience.  
267 Traditionally, ecological resilience measures how fast a system returns to a reference  
268 state following a perturbation. In the context of respiratory pathogens, resilience  
269 measures how fast epidemics return to their endemic cycles after interventions are  
270 lifted.

271 We use an attractor reconstruction approach to quantify how distance from at-  
272 tractor changes over time for each pathogen [18]. We show that the resilience of  
273 a host-pathogen system can be estimated by fitting a linear regression to a logged  
274 distance-from-attractor time series. Overall, we estimate that the resilience for most  
275 common respiratory pathogens ranges between 0.4/year and 1.8/year, which is 3–14  
276 times more resilient than prevaccination measles, indicating potential challenges in  
277 controlling common respiratory pathogens.

278 Our framework allows us to make phenomenological predictions about when each  
279 pathogen will return to their endemic cycles. The ability to predict future epidemic  
280 patterns from resilience estimates offers a new paradigm for epidemic forecasting.  
281 While this approach cannot predict the exact timing of outbreaks or epidemic pat-  
282 terns, it is nonetheless useful for predicting when epidemics will settle down to regular  
283 cycles after a large perturbation, such as COVID-19 interventions.

284 Our analyses suggest a possibility that several pathogens may have converged  
285 to different endemic cycles compared to their pre-pandemic epidemic patterns. Key  
286 examples include human metapnuemovirus, RSV, and bocavirus in Korea as well as

287 RSV in Hong Kong. These changes may reflect changes in surveillance or actual shift  
288 in the dynamics, caused by permanent changes in behavior or population-level immu-  
289 nity. While it seems unlikely that permanent changes in behavior would only affect a  
290 few pathogens and not others, we cannot rule out this possibility given heterogeneity  
291 in the age of infection across different respiratory pathogens [SWP: CITE]. A shift  
292 in population-level immunity is plausible, as the emergence of SARS-CoV-2 and ex-  
293 tinction of influenza B/Yamagata likely caused major changes in immune landscapes;  
294 interactions among co-circulating pathogens, such as cross immunity between RSV  
295 and HMPV [22], may have also contributed to changes in population-level immu-  
296 nity. However, we currently do not know how immunity, or lack thereof, from these  
297 pathogens would affect infection from other pathogens. Future studies should use  
298 detailed mechanistic models, coupled with behavioral and immunological data, to  
299 test these hypotheses and better understand post-pandemic dynamics of endemic  
300 pathogens.

301 We show that susceptible host dynamics shape pathogen resilience, where faster  
302 replenishment of the susceptible population causes the pathogen to be more resilient.  
303 For simplicity, we focus on waning immunity and birth as a main driver of the suscep-  
304 tible host dynamics but other mechanisms can also contribute to the replenishment  
305 of the susceptible population. In particular, pathogen evolution, especially the emer-  
306 gence of antigenically novel strains, can cause effective waning of immunity in the  
307 population; therefore, we hypothesize that faster rates of antigenic evolution can also  
308 cause a pathogen to be more resilient. Future studies should explore the relationship  
309 between the rate of evolution and resilience for antigenically evolving pathogens.

310 Quantifying pathogen resilience also offers novel approaches to validating population-  
311 level epidemiological models. So far, the majority of model validation in epidemiology  
312 is based on the ability of a model to reproduce the observed epidemic dynamics and  
313 to predict future dynamics [23, 22, 24, 25, 26]. However, there can be plethora of  
314 models that meet these criteria. For example, two major RSV models have been pro-  
315 posed so far to explain biennial epidemic patterns: (1) a stage- and age-structured  
316 model that allows for disease severity to vary with number of past infections and  
317 age of infection [24] and (2) a pathogen-interaction model that accounts for cross  
318 immunity between RSV and human metapneumovirus [22]. Since both models can  
319 accurately reproduce the observed epidemic patterns, standard criteria for model  
320 validation do not allow us to distinguish between these two models from population-  
321 level data alone. Instead, we can measure the empirical resilience of each model  
322 by simulating various perturbations and compare them to estimates of empirical re-  
323 siliience from data, using COVID-19 interventions as an opportunity. Future studies  
324 should further investigate using pathogen resilience for validating epidemic models.

325 There are several limitations to our work. First of all, we did not extensively ex-  
326 plore other approaches to reconstructing the attractor. Recent studies showed that  
327 more sophisticated approaches, such as using non-uniform embedding, can provide  
328 more robust reconstruction for noisy data [21]. In the context of causal inference,  
329 choices about embedding can have major impact on the resulting inference [27]. Our

resilience estimates are likely overly confident given a lack of uncertainties in attractor reconstruction as well as the simplicity of our statistical framework. Short pre-pandemic time series also contributes to the crudeness of our estimates. Nonetheless, as illustrated in our sensitivity analyses (Supplementary Figure S6, S10–S12), inferences about pathogen resilience appear to be robust to decisions about embedding lags and dimensions—this is because tracking the rate at which the system approaches the attractor is likely a much simpler problem than making inferences about causal directionality. Our qualitative prediction that common respiratory pathogens are more resilient than prevaccination measles is also likely to be robust to these predictions, given how rapid many respiratory pathogens returned to their original cycles following COVID-19 interventions.

Predicting the impact of anthropogenic changes on infectious disease dynamics is a fundamental aim of infectious disease research in a rapidly changing world. Our study illustrates that quantifying pathogen resilience can help us understand how infectious disease pathogens respond to major perturbations caused by public health interventions. More broadly, a detailed understanding of the determinants of pathogen resilience may offer unique insights into pathogen persistence and controllability.

## Materials and Methods

### Data

We gathered time series on respiratory infections from four different countries: Canada, Hong Kong, Korea, and United States (US). As a reference, we also included time series data on norovirus infections for available countries—in contrast to respiratory pathogens, we expect gastrointestinal viruses, such as norovirus, to be less affected by COVID-19 intervention measures. For all time series, we rounded every year to 52 weeks by taking the average number of cases and tests between the 52nd and 53rd week. We also rescale all time series to account for changes in testing patterns, which are then used for the actual analysis.

Weekly time series of respiratory infection cases in Canada comes from the Respiratory Virus Detection Surveillance System, which collect data from select laboratories across Canada. We extract the data from <https://www.canada.ca/en/public-health/services/surveillance/respiratory-virus-detections-canada.html>. To account for an increase in testing from 2013 to 2024, we calculate a 2 year moving average for the number of tests for each pathogen, which we use as a proxy for testing effort. Then, we divide the smoothed testing patterns by the smoothed value at the final week such that the testing effort has a maximum of 1. We then divide weekly cases by the testing effort to obtain a scaled case time series. A similar approach was used earlier for the analysis of RSV time series in the US [24].

Weekly time series of respiratory infection cases in Hong Kong comes from the Centre for Health Protection, Department of Health. We extract the data from

370 <https://www.chp.gov.hk/en/statistics/data/10/641/642/2274.html>. We also  
371 apply the same scaling procedure to the time series as we did for Canada. For Hong  
372 Kong, we only adjust for testing efforts up to the end of 2019 because there was a  
373 major reduction in testing for common respiratory pathogens since 2020.

374 Weekly time series of acute respiratory infection cases in Korea comes from Ko-  
375 rea Disease Control and Prevention Agency. We extract the data from <https://dportal.kdca.go.kr/pot/is/st/ari.do>. While we do not have information on  
376 testing, the reported number of respiratory infections consistently increased from  
377 2013 to the end of 2019, which we interpreted as changes in testing patterns. Since  
378 we do not have testing numbers, we used the weekly sum of all acute respiratory vi-  
379 ral infection cases as a proxy for testing, which were further smoothed with moving  
380 averaged and scaled to have a maximum of 1. For Korea, we also only adjust for  
381 testing efforts up to the end of 2019.

383 Finally, weekly time series of respiratory infection cases in the US comes from  
384 the National Respiratory and Enteric Virus Surveillance System. In the US, there  
385 has been a large increase in testing against some respiratory pathogens, especially  
386 RSV, which could not be corrected for through simple scaling. Instead, we derive an  
387 incidence proxy by multiplying the test positivity with influenza-like illness positivity,  
388 which is taken from <https://gis.cdc.gov/grasp/fluvview/fluportaldashboard.html>. This method of estimating an incidence proxy has been recently applied in  
389 the analysis of seasonal coronaviruses [6] and Mycoplasma pneumoniae infections [4].  
390 Detailed assumptions and justifications are provided in [28].

## 392 Estimating pathogen resilience

393 In order to measure pathogen resilience from surveillance data, we first reconstruct  
394 the empirical pre-pandemic attractor of the system using Takens' embedding theorem  
395 [18]. Specifically, for a given pathogen, we take the pre-pandemic (before 2020)  
396 case time series  $C(t)$  and reconstruct the attractor using delayed embedding with a  
397 uniform delay of  $\tau$  and dimension  $M$ :

$$X_{\tau,m}(t) = \langle \log(C(t) + 1), \log(C(t - \tau) + 1), \dots, \log(C(t - (M - 1)\tau) + 1) \rangle. \quad (2)$$

398 Here, the delay  $\tau$  is determined by looking at the autocorrelation of the logged pre-  
399 pandemic time series and asking when the autocorrelation crosses 0 for the first time  
400 [21]; a typical delay for an annual outbreak is around 13 weeks.

401 Then, for a given delay  $\tau$ , we determine the embedding dimension  $M$  using the  
402 false nearest neighbors approach [20, 21]. To do so, we start with an embedding  
403 dimension  $e$  and construct a set of points  $A_{\tau,e} = \{X_{\tau,e}(t) | t < 2020\}$ . Then, for  
404 each point  $X_{\tau,e}(t)$ , we determine the nearest neighbor from the set  $A_{\tau,e}$ , which we  
405 denote  $X_{\tau,e}(t_{nn})$  for  $t \neq t_{nn}$ . Then, if the distance between these two points on  $e + 1$   
406 dimension,  $D_{\tau,e+1}(t) = \|X_{\tau,e+1}(t_{nn}) - X_{\tau,e+1}(t)\|_2$ , is larger than their distance on  
407  $e$  dimension,  $D_{\tau,e}(t) = \|X_{\tau,e}(t_{nn}) - X_{\tau,e}(t)\|_2$ , these two points are deemed to be  
408 false nearest neighbors; specifically, we use a threshold  $R$  for the ratio between two

409 distances  $D_{\tau,e+1}(t)/D_{\tau,e}(t)$  to determine false nearest neighbors. In the main text,  
 410 we determine embedding dimension based as the first dimension without any false  
 411 nearest neighbors for  $R = 10$ . In Supplementary Materials, we impose  $R = 5$  to select  
 412 for higher dimensions. Once we determine the embedding lag  $\tau$  and dimension  $M$ ,  
 413 we apply the embedding to the entire time series and calculate the nearest neighbor  
 414 distance against the attractor  $A_{\tau,M}$  to obtain a time series of distance from attractor  
 415  $D_{\tau,M}(t)$ .

416 From a time series of distance from attractor, we estimate pathogen resilience  
 417 by fitting a linear regression to an appropriate window. To automatically select  
 418 the fitting window, we begin by smoothing the distance time series using locally  
 419 estimated scatterplot smoothing (LOESS) to obtain  $\hat{D}_{\tau,M}(t)$ , where the smoothing  
 420 is performed on a log scale and exponentiated afterwards. Then, we determine  
 421 threshold values ( $T_{\text{start}}$  and  $T_{\text{end}}$ ) for the smoothed distances and choose the fitting  
 422 window based on when  $\hat{D}_{\tau,M}(t)$  crosses these threshold values for the first time.  
 423 These thresholds are determined by first calculating maximum distance,

$$\max \hat{D} = \max \hat{D}_{\tau,M}(t), \quad (3)$$

424 and mean pre-pandemic distance,

$$\hat{D}_{\text{mean}} = \frac{1}{N_{t < 2020}} \sum_{t < 2020} \hat{D}_{\tau,M}(t), \quad (4)$$

425 as a reference, and then dividing their ratios into 10 equal bins:

$$T_{\text{start}} = \hat{D}_{\text{mean}} \times \left( \frac{\max \hat{D}}{\hat{D}_{\text{mean}}} \right)^{9/10} \quad (5)$$

$$T_{\text{end}} = \hat{D}_{\text{mean}} \times \left( \frac{\max \hat{D}}{\hat{D}_{\text{mean}}} \right)^{1/10} \quad (6)$$

426 This allows us to discard the initial period during which the distance increases (from  
 427 the introduction of intervention measures) and the final period during which the  
 428 distance plateaus (as the system reaches an attractor). The fitting window is deter-  
 429 mined based on when the smoothed distance  $\hat{D}_{\tau,M}(t)$  crosses these threshold values  
 430 for the first time; then, we fit a linear regression to logged (unsmoothed) distances  
 431  $\log D_{\tau,M}(t)$  using that window.

## 432 Mathematical modeling

433 Throughout the paper, we use a series of mathematical models to illustrate the con-  
 434 cept of pathogen resilience and to understand the determinants of pathogen resilience.  
 435 In general, the intrinsic resilience for a given system is given by the largest real part  
 436 of the eigenvalues of the linearized system at endemic equilibrium. Here, we focus on

437 the SIRS model and present the details of other models in Supplementary Materials.  
 438 The SIRS (Susceptible-Infected-Recovered-Susceptible) model is the simplest model  
 439 that allows for waning of immunity, where recovered (immune) individuals are as-  
 440 sumed to become fully susceptible after an average of  $1/\delta$  time period. The dynamics  
 441 of the SIRS model is described by the following set of differential equations:

$$\frac{dS}{dt} = \mu - \beta(t)SI - \mu S + \delta R \quad (7)$$

$$\frac{dI}{dt} = \beta(t)SI - (\gamma + \mu)I \quad (8)$$

$$\frac{dR}{dt} = \gamma I - (\delta + \mu)R \quad (9)$$

(10)

442 where  $\mu$  represents the birth/death rate,  $\beta(t)$  represents the time-varying trans-  
 443 mission rate, and  $\gamma$  represents the recovery rate. The basic reproduction number  
 444  $\mathcal{R}_0 = \beta(t)/(\gamma + \mu)$  is defined as the average number of secondary infections caused  
 445 by a single infected individual in a fully susceptible population and measures the  
 446 intrinsic transmissibility of a pathogen.

447 When we first introduce the idea of pathogen resilience (Figure 2), we impose  
 448 sinusoidal changes to the transmission rate to account for seasonal transmission:

$$\beta(t) = b_1(1 + \theta \cos(2\pi(t - \phi)))\alpha(t), \quad (11)$$

449 where  $b_1$  represents the baseline transmission rate,  $\theta$  represents the seasonal ampli-  
 450 tude, and  $\phi$  represents the seasonal offset term. Here, we also introduce an extra  
 451 multiplicative term  $\alpha(t)$  to account for the impact of COVID-19 interventions, where  
 452  $\alpha(t) < 1$  indicates transmission reduction. Figure 2A and 2B are generated assuming  
 453  $b_1 = 3 \times (365/7 + 1/50)/\text{years}$ ,  $\theta = 0.2$ ,  $\phi = 0$ ,  $\mu = 1/50/\text{years}$ ,  $\gamma = 365/7/\text{years}$ , and  
 454  $\delta = 1/2/\text{years}$ . In Figure 2A, we impose a 50% transmission reduction for 6 months  
 455 from 2020:

$$\alpha(t) = \begin{cases} 0.5 & 2020 \leq t < 2020.5 \\ 1 & \text{otherwise} \end{cases} \quad (12)$$

456 In Figure 2B, we impose a 50% transmission reduction for 6 months from 2020 and  
 457 a permanent 10% reduction onward:

$$\alpha(t) = \begin{cases} 1 & t < 2020 \\ 0.5 & 2020 \leq t < 2020.5 \\ 0.9 & 2020.5 \leq t \end{cases} \quad (13)$$

458 In both scenarios, we simulate the SIRS model from the following initial conditions  
 459 ( $S(0) = 1/\mathcal{R}_0$ ,  $I(0) = 1 \times 10^{-6}$ , and  $R(0) = 1 - S(0) - I(0)$ ) from 1900 until 2030.

460 To measure the empirical resilience of the SIR model (Figure 2C and 2F), we  
 461 compute the normalized distance between post-intervention susceptible and logged

<sup>462</sup> infected proportions and their corresponding pre-intervention values at the same time  
<sup>463</sup> of year:

$$\sqrt{\left(\frac{S(t) - S_{\text{pre}}(t)}{\sigma_S}\right)^2 + \left(\frac{\log I(t) - \log I_{\text{pre}}(t)}{\sigma_{\log I}}\right)^2}, \quad (14)$$

<sup>464</sup> where  $\sigma_S$  and  $\sigma_{\log I}$  represent the standard deviation in the pre-intervention suscep-  
<sup>465</sup> tible and logged infected proportions. We normalize the differences in susceptible  
<sup>466</sup> and logged infected proportions to allow both quantities to equally contribute to the  
<sup>467</sup> changes in distance from attractor. In Supplementary Materials, we also compare  
<sup>468</sup> the how the degree of seasonal transmission affects empirical resilience by varying  
<sup>469</sup>  $\theta$  from 0 to 0.4; when we assume no seasonality ( $\theta = 0$ ), we do not normalize the  
<sup>470</sup> distance because the standard deviation of pre-intervention dynamics are zero.

<sup>471</sup> Finally, we use the SIRS model to understand how underlying epidemiological  
<sup>472</sup> parameters affect pathogen resilience and link this relationship to underlying sus-  
<sup>473</sup> ceptible host dynamics. For the simple SIRS model without seasonal transmission  
<sup>474</sup> ( $\theta = 0$ ), the intrinsic resilience corresponds to:

$$-\frac{\text{Re}(\lambda)}{2} = \frac{\delta + \beta I^* + \mu}{2}. \quad (15)$$

<sup>475</sup> Here,  $I^*$  represents the prevalence values at endemic equilibrium:

$$I^* = \frac{(\delta + \mu)(\beta - (\gamma + \mu))}{\beta(\delta + \gamma + \mu)}. \quad (16)$$

<sup>476</sup> The susceptible replenishment rate is given by:

$$S_{\text{replenish}} = \frac{\mu + \delta R}{S^*}, \quad (17)$$

<sup>477</sup> where  $S^* = 1/\mathcal{R}_0$  represents the equilibrium proportion of susceptible individuals.  
<sup>478</sup> We vary the basic reproduction number  $\mathcal{R}_0$  between 1.1 to 6 and the average duration  
<sup>479</sup> of immunity  $1/\delta$  between 2 to 80 years, and compute these two quantities. In doing  
<sup>480</sup> so, we fix all other parameters:  $\mu = 1/80/\text{years}$  and  $\gamma = 365/7/\text{years}$ .

481 **Supplementary Text**

482 **Resilience of a stage-structured system.**

483 In Figure 2G–I, we use a more realistic, stage-structured model to illustrate how  
 484 transient phenomena can cause the system to slow down. Specifically, we use the  
 485 stage-structured RSV model proposed by [24], which assumes that subsequent rein-  
 486 fections cause an individual to become less susceptible and transmissible than previ-  
 487 ous infections. The model dynamics can be described as follows:

$$\frac{dM}{dt} = \mu - (\omega + \mu)M \quad (S1)$$

$$\frac{dS_0}{dt} = \omega M - (\lambda(t) + \mu)S_0 \quad (S2)$$

$$\frac{dI_1}{dt} = \lambda(t)S_0 - (\gamma_1 + \mu)I_1 \quad (S3)$$

$$\frac{dS_1}{dt} = \gamma_1 I_1 - (\sigma_1 \lambda(t) + \mu)S_1 \quad (S4)$$

$$\frac{dI_2}{dt} = \sigma_1 \lambda(t)S_1 - (\gamma_2 + \mu)I_2 \quad (S5)$$

$$\frac{dS_2}{dt} = \gamma_2 I_2 - (\sigma_2 \lambda(t) + \mu)S_2 \quad (S6)$$

$$\frac{dI_3}{dt} = \sigma_2 \lambda(t)S_2 - (\gamma_3 + \mu)I_3 \quad (S7)$$

$$\frac{dS_3}{dt} = \gamma_3 I_3 - (\sigma_3 \lambda(t) + \mu)S_3 + \gamma_4 I_4 \quad (S8)$$

$$\frac{dI_4}{dt} = \sigma_3 \lambda(t)S_3 - (\gamma_4 + \mu)I_4 \quad (S9)$$

(S10)

488 where  $M$  represents the proportion of individuals who are maternally immune;  $S_i$   
 489 represents the proportion of individuals who are susceptible after  $i$  prior infections;  $I_i$   
 490 represents the proportion of individuals who are currently (re)-infected with their  $i$ -th  
 491 infection;  $\mu$  represents the birth and death rates;  $1/\omega$  represents the mean duration  
 492 of maternal immunity;  $1/\gamma_i$  represents the mean duration of infection;  $\lambda(t)$  represents  
 493 the force of infection; and  $\sigma_i$  represents the reduction in susceptibility for reinfection.  
 494 The force of infection is modeled using a sinusoidal function:

$$\beta(t) = b_1(1 + \theta \cos(2\pi(t - \phi)))\alpha(t) \quad (S11)$$

$$\lambda(t) = \beta(I_1 + \rho_1 I_2 + \rho_2(I_3 + I_4)), \quad (S12)$$

495 where  $b_1$  represents the baseline transmission rate;  $\theta$  represents the seasonal ampli-  
 496 tude;  $\phi$  represents the seasonal offset term;  $\alpha(t)$  represents the intervention effect;  
 497 and  $\rho_i$  represents the impact of immunity on transmission reduction. We use the

498 following parameters to simulate the impact of interventions on epidemic dynam-  
 499 ics [24]:  $b_1 = 9 \times (365/10 + 1/80)/\text{years}$ ,  $\theta = 0.2$ ,  $\phi = -0.1$ ,  $\omega = 365/112/\text{years}$ ,  
 500  $\gamma_1 = 365/10/\text{years}$ ,  $\gamma_2 = 365/7/\text{years}$ ,  $\gamma_3 = 365/5/\text{years}$ ,  $\sigma_1 = 0.76$ ,  $\sigma_2 = 0.6$ ,  
 501  $\sigma_3 = 0.4$ ,  $\rho_1 = 0.75$ ,  $\rho_2 = 0.51$ , and  $\mu = 1/80/\text{years}$ . We assume a 50% transmission  
 502 reduction for 6 months from 2020:

$$\alpha(t) = \begin{cases} 0.5 & 2020 \leq t < 2020.5 \\ 1 & \text{otherwise} \end{cases} \quad (\text{S13})$$

503 The model is simulated from 1900 to 2030 using the following initial conditions:  
 504  $M = 0$ ,  $S_0 = 1/\mathcal{R}_0 - I_1$ ,  $I_1 = 1 \times 10^{-6}$ ,  $S_1 = 1 - 1/\mathcal{R}_0$ ,  $I_2 = 0$ ,  $S_2 = 0$ ,  $I_3 = 0$ ,  
 505  $S_3 = 0$ , and  $I_4 = 0$ . For the phase plane analysis (Figure 2H) and distance analysis  
 506 (Figure 2I), we rely on the average susceptibility,

$$\bar{S} = S_0 + \sigma_1 S_1 + \sigma_2 S_2 + \sigma_3 S_3, \quad (\text{S14})$$

507 and total prevalence,

$$I_{\text{total}} = I_1 + I_2 + I_3 + I_4. \quad (\text{S15})$$

508 These quantities are used to compute the normalized distance from the attractor, as  
 509 described in the main text.

## 510 Resilience of a multistrain system.

511 We use a simple two-strain model to show that a multistrain host-pathogen system  
 512 that is coupled through cross immunity can be described by a single resilience value.  
 513 The model dynamics can be described as follows [22]:

$$\frac{dS}{dt} = \mu - \mu S - (\lambda_1 + \lambda_2)S + \rho_1 R_1 + \rho_2 R_2 \quad (\text{S16})$$

$$\frac{dI_1}{dt} = \lambda_1 S - (\gamma_1 + \mu)I_1 \quad (\text{S17})$$

$$\frac{dI_2}{dt} = \lambda_2 S - (\gamma_2 + \mu)I_2 \quad (\text{S18})$$

$$\frac{dR_1}{dt} = \gamma_1 I_1 - \lambda_2 \epsilon_{21} R_1 - \rho_1 R_1 + \rho_2 R - \mu R_1 \quad (\text{S19})$$

$$\frac{dR_2}{dt} = \gamma_2 I_2 - \lambda_1 \epsilon_{12} R_2 - \rho_2 R_2 + \rho_1 R - \mu R_2 \quad (\text{S20})$$

$$\frac{dJ_1}{dt} = \lambda_1 \epsilon_{12} R_2 - (\gamma_1 + \mu) J_1 \quad (\text{S21})$$

$$\frac{dJ_2}{dt} = \lambda_2 \epsilon_{21} R_1 - (\gamma_2 + \mu) J_2 \quad (\text{S22})$$

$$\frac{dR}{dt} = \gamma_1 J_1 + \gamma_2 J_2 - \rho_1 R - \rho_2 R - \mu R \quad (\text{S23})$$

514 where  $S$  represents the proportion of individuals who are fully susceptible to infections  
 515 by both strains;  $I_1$  represents the proportion of individuals who are infected with strain 1 without prior immunity;  $I_2$  represents the proportion of individuals who are infected with strain 2 without prior immunity;  $R_1$  represents the proportion of individuals who are fully immune against strain 1 and partially susceptible to reinfection by strain 2;  $R_2$  represents the proportion of individuals who are fully immune against strain 2 and partially susceptible to reinfection by strain 1;  $J_1$  represents the proportion of individuals who are infected with strain 1 with prior immunity against strain 2;  $J_2$  represents the proportion of individuals who are infected with strain 2 with prior immunity against strain 1;  $R$  represents the proportion of individuals who are immune to infections from both strains;  $\mu$  represents the birth/death rate;  $\lambda_1$  and  $\lambda_2$  represent the force of infection from strains 1 and 2, respectively;  $\rho_1$  and  $\rho_2$  represent the waning immunity rate;  $\gamma_1$  and  $\gamma_2$  represent the recovery rate;  $\epsilon_{12}$  and  $\epsilon_{21}$  represent the susceptibility to reinfection with strains 2 and 1, respectively, given prior immunity from infection with strains 1 and 2, respectively. The force of infection is modeled as follows:

$$\beta_1 = b_1(1 + \theta_1 \sin(2\pi(t - \phi_1)))\alpha(t) \quad (\text{S24})$$

$$\beta_2 = b_2(1 + \theta_2 \sin(2\pi(t - \phi_2)))\alpha(t) \quad (\text{S25})$$

$$\lambda_1 = \beta_1(I_1 + J_1) \quad (\text{S26})$$

$$\lambda_2 = \beta_2(I_2 + J_2) \quad (\text{S27})$$

530 In Supplementary Figures S2–S4, we assume the following parameters:  $b_1 = 2 \times$   
 531  $52/\text{years}$ ,  $b_2 = 4 \times 52/\text{years}$ ,  $\phi_1 = \phi_2 = 0$ ,  $\epsilon_{12} = 0.9$ ,  $\epsilon_{21} = 0.5$ ,  $\gamma_1 = \gamma_2 = 52/\text{years}$ ,  
 532  $\rho_1 = \rho_2 = 1/\text{years}$ , and  $\mu = 1/70/\text{years}$ . For all simulations, we assume a 50%  
 533 transmission reduction for 6 months from 2020:

$$\alpha(t) = \begin{cases} 0.5 & 2020 \leq t < 2020.5 \\ 1 & \text{otherwise} \end{cases} \quad (\text{S28})$$

534 The seasonal amplitude  $\theta$  is varied from 0 to 0.4. All simulations are ran from 1900  
 535 to 2030 from the following initial conditions:  $S(0) = 1 - 2 \times 10^{-6}$ ,  $I_1(0) = 1 \times 10^{-6}$ ,  
 536  $I_2(0) = 1 \times 10^{-6}$ ,  $R_1(0) = 0$ ,  $R_2(0) = 0$ ,  $J_1(0) = 0$ ,  $J_2(0) = 0$ , and  $R(0) = 0$ .

537 For this, we consider three different scenarios for measuring pathogen resilience:  
 538 (1) we only have information about strain 1, (2) we only have information about  
 539 strain 2, and (3) we are unable to distinguish the differences between strains. In  
 540 the first two scenarios (see panels A–C for strain 1 and panels D–F for strain 2), we  
 541 consider the dynamics of average susceptibility for each strain and total prevalence:

$$\bar{S}_1 = S + \epsilon_{12}R_2 \quad (\text{S29})$$

$$\hat{I}_1 = I_1 + J_1 \quad (\text{S30})$$

$$\bar{S}_2 = S + \epsilon_{21}R_1 \quad (\text{S31})$$

$$\hat{I}_2 = I_2 + J_2 \quad (\text{S32})$$

<sup>542</sup> In the third scenario (panels G–I), we consider the dynamics of total susceptible and  
<sup>543</sup> infected population:

$$\hat{S} = S + R_2 + R_1 \quad (\text{S33})$$

$$\hat{I} = I_1 + J_1 + I_2 + J_2 \quad (\text{S34})$$

$$(\text{S35})$$

<sup>544</sup> These quantities are used to compute the normalized distance from the attractor, as  
<sup>545</sup> described in the main text.

## <sup>546</sup> Estimating intrinsic resilience using mechanistic model

<sup>547</sup> We test whether we can reliably estimate the intrinsic resilience of a system by fitting  
<sup>548</sup> a mechanistic model. Specifically, we simulate case time series from stochastic SIRS  
<sup>549</sup> and two-strain models and fit a simple, deterministic SIRS model using a Bayesian  
<sup>550</sup> framework.

<sup>551</sup> First, we describe the simulation set up. The stochastic SIRS model can be  
<sup>552</sup> written as follows:

$$\beta(t) = \mathcal{R}_0 \left( 1 + \theta \cos \left( \frac{2\pi t}{364} \right) \right) \alpha(t)(1 - \exp(-\gamma)) \quad (\text{S36})$$

$$\text{FOI}(t) = \beta(t)I(t - \Delta t)/N \quad (\text{S37})$$

$$B(t) \sim \text{Poisson}(\mu N) \quad (\text{S38})$$

$$\Delta S(t) \sim \text{Binom}(S(t - \Delta t), 1 - \exp(-(\text{FOI}(t) + \mu)\Delta t)) \quad (\text{S39})$$

$$N_{SI}(t) \sim \text{Binom}\left(\Delta S(t), \frac{\text{FOI}(t)}{\text{FOI}(t) + \mu}\right) \quad (\text{S40})$$

$$\Delta I(t) \sim \text{Binom}(I(t - \Delta t), 1 - \exp(-(\gamma + \mu)\Delta t)) \quad (\text{S41})$$

$$N_{IR}(t) \sim \text{Binom}\left(\Delta I(t), \frac{\gamma}{\gamma + \mu}\right) \quad (\text{S42})$$

$$\Delta R(t) \sim \text{Binom}(R(t - \Delta t), 1 - \exp(-(\delta + \mu)\Delta t)) \quad (\text{S43})$$

$$N_{RS}(t) \sim \text{Binom}\left(\Delta R(t), \frac{\delta}{\delta + \mu}\right) \quad (\text{S44})$$

$$S(t) = S(t - \Delta t) + N_{RS}(t) + B(t) - \Delta S(t) \quad (\text{S45})$$

$$I(t) = I(t - \Delta t) + N_{SI}(t) - \Delta I(t) \quad (\text{S46})$$

$$R(t) = R(t - \Delta t) + N_{IR}(t) - \Delta R(t) \quad (\text{S47})$$

<sup>553</sup> where FOI represent the force of infection;  $N_{ij}$  represent the number of individuals  
<sup>554</sup> moving from compartment  $i$  to  $j$  on a given day; and  $B(t)$  represents the number  
<sup>555</sup> of new births. We simulate the model on a daily scale—assuming 364 days in a  
<sup>556</sup> year so that it can be evenly grouped into 52 weeks—with the following parameters:  
<sup>557</sup>  $\mathcal{R}_0 = 3$ ,  $\theta = 0.1$ ,  $\gamma = 1/7/\text{days}$ ,  $\delta = 1/(364 \times 2)/\text{days}$ ,  $\mu = 1/(364 \times 50)/\text{days}$ , and

558  $N = 1 \times 10^8$ . The model is simulated from 1900 to 2030 assuming  $S(0) = N/3$ ,  
 559  $I(0) = 100$ , and  $R(0) = N - S(0) - I(0)$ . The observed incidence from the model is  
 560 then simulated as follows:

$$C(t) = \text{Beta} - \text{Binom}(N_{SI}(t), \rho, k), \quad (\text{S48})$$

561 where  $\rho$  represents the reporting probability and  $k$  represents the overdispersion pa-  
 562 rameter of beta-binomial distribution. We assume  $\rho = 0.002$  (i.e., 0.2% probability)  
 563 and  $k = 1000$ .

564 The stochastic two-strain model can be written as follows:

$$\beta_1(t) = b_1 \left( 1 + \theta_1 \cos \left( \frac{2\pi(t - \phi_1)}{364} \right) \right) \alpha(t) \quad (\text{S49})$$

$$\beta_2(t) = b_2 \left( 1 + \theta_2 \cos \left( \frac{2\pi(t - \phi_2)}{364} \right) \right) \alpha(t) \quad (\text{S50})$$

$$\text{FOI}_1(t) = \beta_1(t)(I_1(t - \Delta t) + J_1(t - \Delta t))/N \quad (\text{S51})$$

$$\text{FOI}_2(t) = \beta_2(t)(I_2(t - \Delta t) + J_2(t - \Delta t))/N \quad (\text{S52})$$

$$B(t) \sim \text{Poisson}(\mu N) \quad (\text{S53})$$

$$\Delta S(t) \sim \text{Binom}(S(t - \Delta t), 1 - \exp(-(\text{FOI}_1(t) + \text{FOI}_2(t) + \mu)\Delta t)) \quad (\text{S54})$$

$$N_{SI_1}(t) \sim \text{Binom}\left(\Delta S(t), \frac{\text{FOI}_1(t)}{\text{FOI}_1(t) + \text{FOI}_2(t) + \mu}\right) \quad (\text{S55})$$

$$N_{SI_2}(t) \sim \text{Binom}\left(\Delta S(t), \frac{\text{FOI}_2(t)}{\text{FOI}_1(t) + \text{FOI}_2(t) + \mu}\right) \quad (\text{S56})$$

$$\Delta I_1(t) \sim \text{Binom}(I_1(t - \Delta t), 1 - \exp(-(\gamma_1 + \mu)\Delta t)) \quad (\text{S57})$$

$$N_{I_1 R_1}(t) \sim \text{Binom}\left(\Delta I_1(t), \frac{\gamma_1}{\gamma_1 + \mu}\right) \quad (\text{S58})$$

$$\Delta I_2(t) \sim \text{Binom}(I_2(t - \Delta t), 1 - \exp(-(\gamma_2 + \mu)\Delta t)) \quad (\text{S59})$$

$$N_{I_2 R_2}(t) \sim \text{Binom}\left(\Delta I_2(t), \frac{\gamma_2}{\gamma_2 + \mu}\right) \quad (\text{S60})$$

$$\Delta R_1(t) \sim \text{Binom}(R_1(t - \Delta t), 1 - \exp(-(\epsilon_{21}\text{FOI}_2(t) + \rho_1 + \mu)\Delta t)) \quad (\text{S61})$$

$$N_{R_1 S}(t) \sim \text{Binom}\left(\Delta R_1(t), \frac{\rho_1}{\epsilon_{21}\text{FOI}_2(t) + \rho_1 + \mu}\right) \quad (\text{S62})$$

$$N_{R_1 J_2}(t) \sim \text{Binom}\left(\Delta R_1(t), \frac{\epsilon_{21}\text{FOI}_2(t)}{\epsilon_{21}\text{FOI}_2(t) + \rho_1 + \mu}\right) \quad (\text{S63})$$

$$\Delta R_2(t) \sim \text{Binom}(R_2(t - \Delta t), 1 - \exp(-(\epsilon_{12}\text{FOI}_1(t) + \rho_2 + \mu)\Delta t)) \quad (\text{S64})$$

$$N_{R_2 S}(t) \sim \text{Binom}\left(\Delta R_2(t), \frac{\rho_2}{\epsilon_{12}\text{FOI}_1(t) + \rho_2 + \mu}\right) \quad (\text{S65})$$

$$N_{R_2 J_1}(t) \sim \text{Binom}\left(\Delta R_2(t), \frac{\epsilon_{12}\text{FOI}_1(t)}{\epsilon_{12}\text{FOI}_1(t) + \rho_2 + \mu}\right) \quad (\text{S66})$$

$$\Delta J_1(t) \sim \text{Binom}(J_1(t - \Delta t), 1 - \exp(-(\gamma_1 + \mu)\Delta t)) \quad (\text{S67})$$

$$N_{J_1R}(t) \sim \text{Binom}\left(\Delta J_1(t), \frac{\gamma_1}{\gamma_1 + \mu}\right) \quad (\text{S68})$$

$$\Delta J_2(t) \sim \text{Binom}(J_2(t - \Delta t), 1 - \exp(-(\gamma_2 + \mu)\Delta t)) \quad (\text{S69})$$

$$N_{J_2R}(t) \sim \text{Binom}\left(\Delta J_2(t), \frac{\gamma_2}{\gamma_2 + \mu}\right) \quad (\text{S70})$$

$$\Delta R(t) \sim \text{Binom}(R(t - \Delta t), 1 - \exp(-(\rho_1 + \rho_2 + \mu)\Delta t)) \quad (\text{S71})$$

$$N_{RR_1}(t) \sim \text{Binom}\left(\Delta R(t), \frac{\rho_1}{\rho_1 + \rho_2 + \mu}\right) \quad (\text{S72})$$

$$N_{RR_2}(t) \sim \text{Binom}\left(\Delta R(t), \frac{\rho_2}{\rho_1 + \rho_2 + \mu}\right) \quad (\text{S73})$$

$$S(t) = S(t - \Delta t) - \Delta S(t) + B(t) + N_{R_1S}(t) + N_{R_2S}(t) \quad (\text{S74})$$

$$I_1(t) = I_1(t - \Delta t) - \Delta I_1(t) + N_{SI_1}(t) \quad (\text{S75})$$

$$I_2(t) = I_2(t - \Delta t) - \Delta I_2(t) + N_{SI_2}(t) \quad (\text{S76})$$

$$R_1(t) = R_1(t - \Delta t) - \Delta R_1(t) + N_{I_1R_1}(t) + N_{RR_1}(t) \quad (\text{S77})$$

$$R_2(t) = R_2(t - \Delta t) - \Delta R_2(t) + N_{I_2R_2}(t) + N_{RR_2}(t) \quad (\text{S78})$$

$$J_1(t) = J_1(t - \Delta t) - \Delta J_1(t) + N_{R_2J_1}(t) \quad (\text{S79})$$

$$J_2(t) = J_2(t - \Delta t) - \Delta J_2(t) + N_{R_1J_2}(t) \quad (\text{S80})$$

$$R(t) = R(t - \Delta t) - \Delta R(t) + N_{J_1R}(t) + N_{J_2R}(t) \quad (\text{S81})$$

565 We simulate the model on a daily scale with previously estimated parameters for the  
 566 RSV-HMPV interaction [22]:  $b_1 = 1.7/\text{weeks}$ ,  $b_2 = 1.95/\text{weeks}$ ,  $\theta_1 = 0.4$ ,  $\theta_2 = 0.3$ ,  
 567  $\phi_1 = 0.005 \times 7/364$ ,  $\phi_2 = 4.99 \times 7/364$ ,  $\epsilon_{12} = 0.92$ ,  $\epsilon_{21} = 0.45$ ,  $\gamma_1 = 1/10/\text{days}$ ,  
 568  $\gamma_2 = 1/10/\text{days}$ ,  $\rho_1 = 1/364/\text{days}$ ,  $\rho_2 = 1/364/\text{days}$ ,  $\mu = 1/(70 \times 364)/\text{days}$ , and  
 569  $N = 1 \times 10^8$ . The model is simulated from 1900 to 2030 assuming  $S(0) = N - 200$ ,  
 570  $I_1(0) = 100$ ,  $I_2(0) = 100$ ,  $R_1(0) = 0$ ,  $R_2(0) = 0$ ,  $J_1(0) = 0$ ,  $J_2(0) = 0$ , and  $R(0) = 0$ .  
 571 The observed incidence for each strain is then simulated as follows:

$$C_1(t) = \text{Beta} - \text{Binom}(N_{SI_1}(t) + N_{R_2J_1}, \rho, k), \quad (\text{S82})$$

$$C_2(t) = \text{Beta} - \text{Binom}(N_{SI_2}(t) + N_{R_1J_2}, \rho, k), \quad (\text{S83})$$

572 where  $\rho$  represents the reporting probability and  $k$  represents the overdispersion pa-  
 573 rameter of beta-binomial distribution. We assume  $\rho = 0.002$  (i.e., 0.2% probability)  
 574 and  $k = 500$ . We also consider the total incidence:  $C_{\text{total}}(t) = C_1(t) + C_2(t)$ .

575 For both models, we consider a more realistic challenges in intervention effects  
 576  $\alpha(t)$  to challenge our ability to estimate the intervention effects. Thus, we assume  
 577 a 40% transmission reduction for 3 months from March 2020, followed by a 10%  
 578 transmission reduction for 6 months, 20% transmission reduction for 3 months, and

579 a final return to normal levels:

$$\alpha(t) = \begin{cases} 1 & t < 2020.25 \\ 0.6 & 2020.25 \leq t < 2020.5 \\ 0.9 & 2020.5 \leq t < 2021 \\ 0.8 & 2021 \leq t < 2021.25 \\ 1 & 2021.25 \leq t \end{cases}. \quad (\text{S84})$$

580 For all simulations, we truncate the time series from the beginning of 2014 to the  
581 end of 2023 and aggregate them into weekly cases.

582 To infer intrinsic resilience from time series, we fit a simple discrete time, deter-  
583 ministic SIRS model [4]:

$$\Delta t = 1 \text{ week} \quad (\text{S85})$$

$$\text{FOI}(t) = \beta(t)(I(t - \Delta t) + \omega)/N \quad (\text{S86})$$

$$\Delta S(t) = [1 - \exp(-(\text{FOI}(t) + \mu)\Delta t)] S(t - \Delta t) \quad (\text{S87})$$

$$N_{SI}(t) = \frac{\text{FOI}(t)\Delta S(t)}{\text{FOI}(t) + \mu} \quad (\text{S88})$$

$$\Delta I(t) = [1 - \exp(-(\gamma + \mu)\Delta t)] I(t - \Delta t) \quad (\text{S89})$$

$$N_{IR}(t) = \frac{\gamma \Delta I(t)}{\gamma + \mu} \quad (\text{S90})$$

$$\Delta R(t) = [1 - \exp(-(\nu + \mu)\Delta t)] R(t - \Delta t) \quad (\text{S91})$$

$$N_{RS}(t) = \frac{\nu \Delta R(t)}{\nu + \mu} \quad (\text{S92})$$

$$S(t) = S(t - \Delta t) + \mu S - \Delta S(t) + N_{RS}(t) \quad (\text{S93})$$

$$I(t) = I(t - \Delta t) - \Delta I(t) + N_{SI}(t) \quad (\text{S94})$$

$$R(t) = R(t - \Delta t) - \Delta R(t) + N_{IR}(t) \quad (\text{S95})$$

584 where we include an extra term  $\omega$  to account for external infections. Although actual  
585 simulations do not include any external infections, we found that including this term  
586 generally helped with model convergence in previous analyses [4]. The transmission  
587 rate is divided into a seasonal term  $\beta_{\text{seas}}(t)$  (repeated every year) and intervention  
588 term  $\alpha(t)$ , which are estimated jointly:

$$\beta(t) = \beta_{\text{seas}}(t)\alpha(t), \quad (\text{S96})$$

589 where  $\alpha < 1$  corresponds to reduction in transmission due to intervention effects. To  
590 constrain the smoothness of  $\beta_{\text{seas}}(t)$ , we impose cyclic, random-walk priors:

$$\beta_{\text{seas}}(t) \sim \text{Normal}(\beta_{\text{seas}}(t - 1), \sigma) \quad t = 2 \dots 52 \quad (\text{S97})$$

$$\beta_{\text{seas}}(1) \sim \text{Normal}(\beta_{\text{seas}}(52), \sigma) \quad (\text{S98})$$

591 [SWP: I noticed that I forgot to put a prior on  $\sigma$  so need to re-do this but won't  
 592 change the results.] We fix  $\alpha(t) = 1$  for all  $t < 2020$  and estimate  $\alpha$  assuming a  
 593 normal prior:

$$\alpha \sim \text{Normal}(1, 0.25). \quad (\text{S99})$$

594 We assume weakly informative priors on  $\omega$  and  $\tau$ :

$$\omega \sim \text{Normal}(0, 200) \tau \sim \text{Normal}(104, 26) \quad (\text{S100})$$

595 We assume that the true birth/death rates, population sizes, and recovery rates are  
 596 known. We note, however, that assuming  $\gamma = 1/\text{week}$  actually correspond to a  
 597 mean infectious period of 1.6 weeks, which is much longer than the true value; this  
 598 approximation allows us to test whether we can still robustly estimate the intrinsic  
 599 resilience given parameters mis-specification. Initial conditions are estimated with  
 600 following priors:

$$S(0) = Ns(0) \quad (\text{S101})$$

$$I(0) = Ni(0) \quad (\text{S102})$$

$$s(0) \sim \text{Uniform}(0, 1) \quad (\text{S103})$$

$$i(0) \sim \text{Half-Normal}(0, 0.001) \quad (\text{S104})$$

601 Finally, the Observation model is specified as follows:

$$\text{Cases}(t) \sim \text{Negative-Binomial}(\rho N_{SI}(t), \phi) \quad (\text{S105})$$

$$\rho \sim \text{Half-Normal}(0, 0.02) \quad (\text{S106})$$

$$\phi \sim \text{Half-Normal}(0, 10) \quad (\text{S107})$$

602 where  $\rho$  represents the reporting probability and  $\phi$  represents the negative binomial  
 603 overdispersion parameter.

604 The model is fitted to four separate time series: (1) incidence time series from  
 605 the SIRS model, (2) incidence time series for strain 1 from the two-strain model,  
 606 (3) incidence time series for strain 2 from the two-strain model, and (4) combined  
 607 incidence time series for strains 1 and 2 from the two-strain model. The model was  
 608 fitted using rstan [29, 30]. The resulting posterior distribution was used to calculate  
 609 the intrinsic resilience of the seasonally unforced system with the same parameters;  
 610 eigenvalues of the discrete-time SIR model were computed by numerically finding  
 611 the equilibrium and calculating the Jacobian matrix.

## 612 **Validations for window-selection criteria**

613 We use stochastic SIRS simulations to validate the window-selection criteria that we  
 614 use for the linear regression for estimating empirical resilience. For each simulation,  
 615 we begin by generating a random intervention  $\alpha(t)$  from random set of parameters.  
 616 First, we draw the duration of intervention  $\tau_{\text{np}}^*$  from a uniform distribution between

617 0.5 and 3.5 years. Then, we draw independent normal variables  $z_i$  of length  $\lfloor 364\tau_{\text{npi}} \rfloor$   
 618 with a standard deviation of 0.02 and take a reverse cumulative sum to obtain a  
 619 realistic shape for the intervention:

$$x_n = 1 + \sum_{i=n}^{\lfloor 364\tau_{\text{npi}} \rfloor} z_i, \quad n = 1, \dots, \lfloor 364\tau_{\text{npi}} \rfloor. \quad (\text{S108})$$

620 We repeat this random generation process until less than 10% of  $x_n$  exceeds 1. Then,  
 621 we set any values that are above 1 or below 0 as 1 and 0, respectively. Then, we  
 622 randomly draw the minimum transmission during intervention  $\alpha_{\min}$  from a uniform  
 623 distribution between 0.5 and 0.7 and scale  $x_n$  to have a minimum of  $\alpha_{\min}$ :

$$x_{\text{scale},n} = \alpha_{\min} + (1 - \alpha_{\min}) \times \frac{x_n - \min x_n}{1 - \min x_n}. \quad (\text{S109})$$

624 This allows us to simulate a realistically shaped interventions:

$$\alpha(t) = \begin{cases} 1 & t < 2020 \\ x_{\text{scale},364(t-2020)} & 2020 \leq t < 2020 + \tau_{\text{npi}} \\ 1 & \tau_{\text{npi}} \leq t \end{cases}. \quad (\text{S110})$$

625 Given this intervention function, we draw  $\mathcal{R}_0$  from a uniform distribution between 1.5  
 626 and 3 and the mean duration of immunity  $1/\delta$  from a uniform distribution between  
 627 0.5 and 2. Then, we simulate the stochastic SIRS model from  $S(0) = 10^8/\mathcal{R}_0$  and  
 628  $I(0) = 100$  from 1990 to 2025 and truncate the time series to 2014–2025; if the  
 629 epidemic becomes extinct before the end of simulation, we discard that simulation  
 630 and start over from the intervention generation step. We then apply the window  
 631 selection criteria described in the main text to compute the empirical resilience and  
 632 compare it against the intrinsic resilience of the seasonally unforced system. We also  
 633 compare this with the naive approach that uses the entire distance-from-attractor  
 634 time series, starting from the maximum distance. We repeat this procedure 500  
 635 times and quantify the correlation between empirical and intrinsic resilience estimates  
 636 across two approaches.

# Supplementary Figures

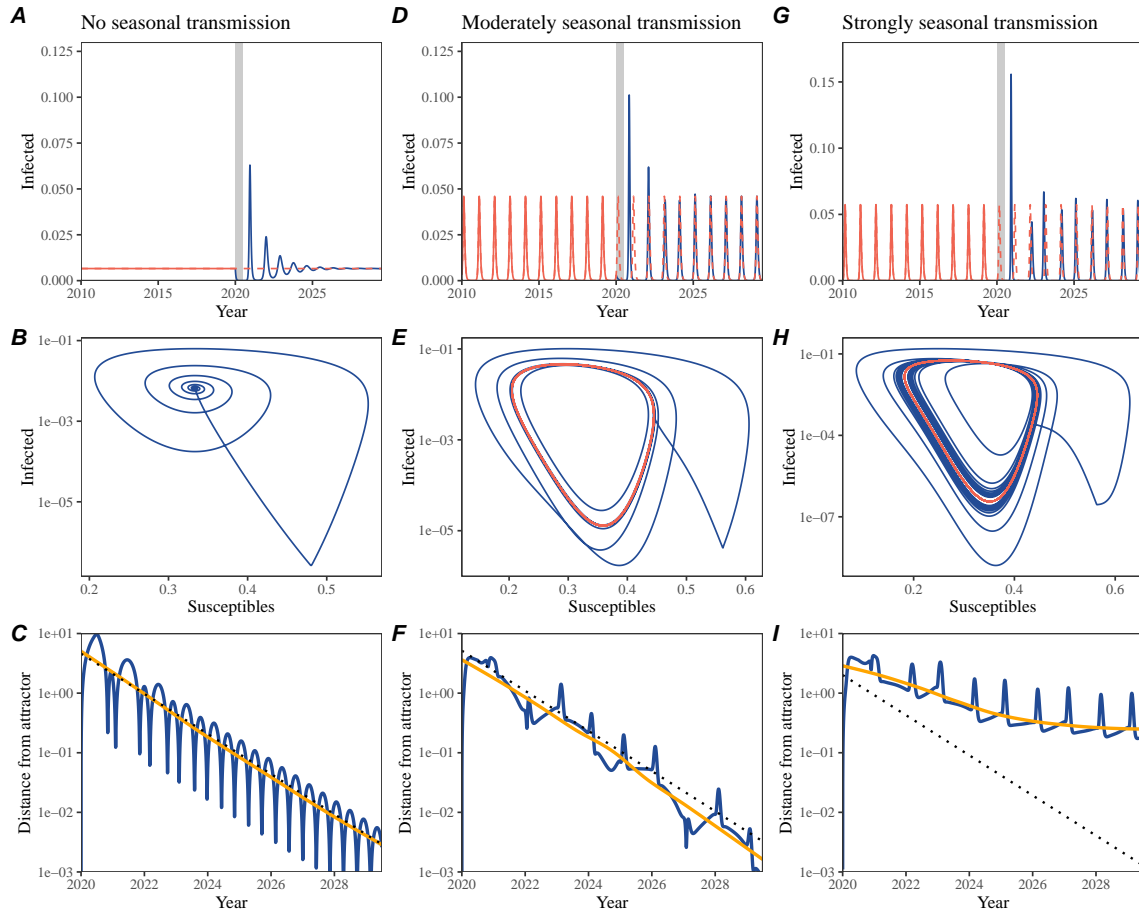


**Figure S1: Impact of seasonal transmission on pathogen resilience.** (A, D, G) Simulated epidemic trajectories using the SIRS model without seasonal forcing (A), with seasonal forcing of amplitude of 0.2 (D), and with seasonal forcing of amplitude of 0.2 (G). Red and blue solid lines represent epidemic dynamics before and after interventions are introduced, respectively. Red dashed lines represent counterfactual epidemic dynamics in the absence of interventions. Gray regions indicate the duration of interventions. (B, E, H) Phase plane representation of the corresponding model. Red and blue solid lines represent epidemic trajectories on an SI phase plane before and after interventions are introduced, respectively. (C, F, I) Changes in logged distance from attractor over time. Blue lines represent the logged distance from attractor. Orange lines represent the locally estimated scatterplot smoothing (LOESS) fits to the logged distance from attractor. Dotted lines are superimposed as a comparison to have the same slope as the intrinsic resilience of the seasonally unforced system.

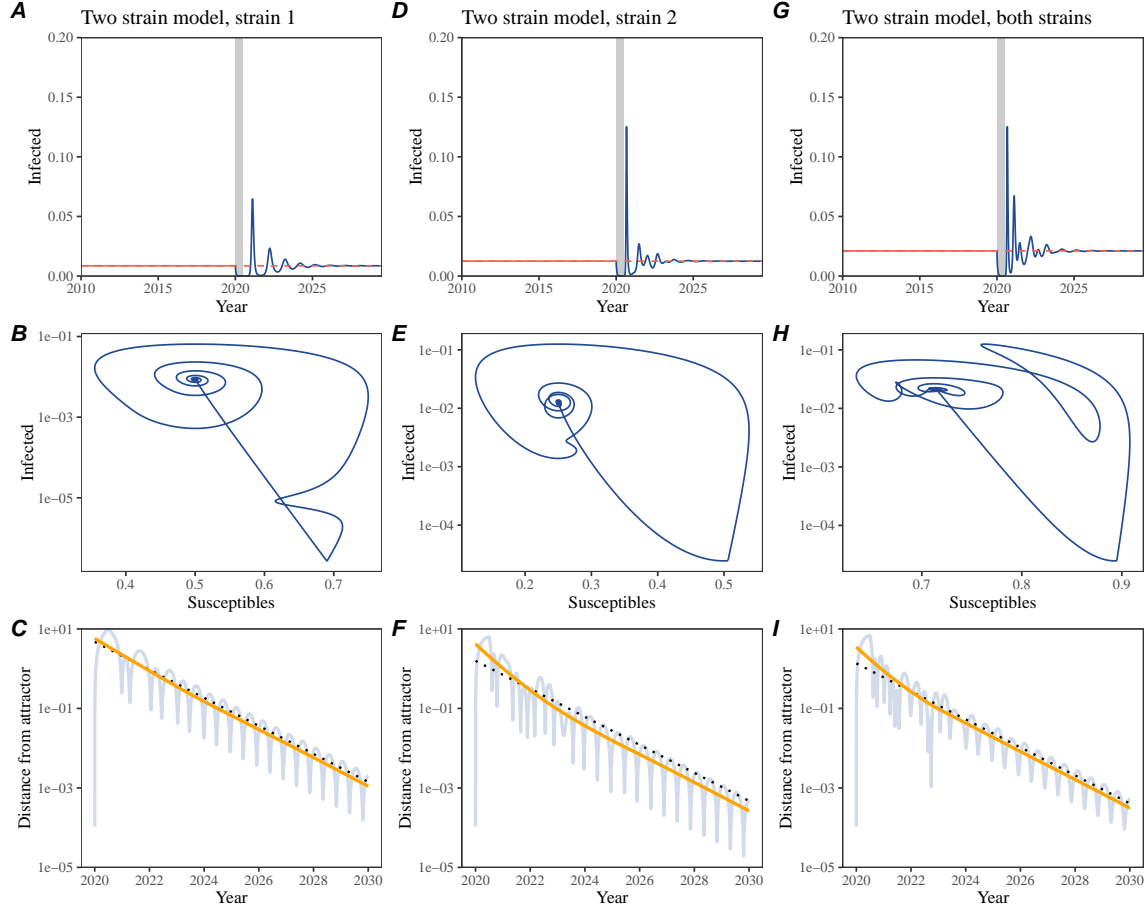


**Figure S2: Conceptual framework for measuring pathogen resilience following NPIs for a multi-strain system without seasonal forcing.** (A, D, G) Simulated epidemic trajectories using a multi-strain system without seasonal forcing. Red and blue solid lines represent epidemic dynamics before and after interventions are introduced, respectively. Red dashed lines represent counterfactual epidemic dynamics in the absence of interventions. Gray regions indicate the duration of interventions. (B, E, H) Phase plane representation of the corresponding model. Red and blue solid lines represent epidemic trajectories on an SI phase plane before and after interventions are introduced, respectively. (C, F, I) Changes in logged distance from attractor over time. Blue lines represent the logged distance from attractor. Orange lines represent the locally estimated scatterplot smoothing (LOESS) fits to the logged distance from attractor. Dotted lines are superimposed as a comparison to have the same slope as the intrinsic resilience of the seasonally unforced system.

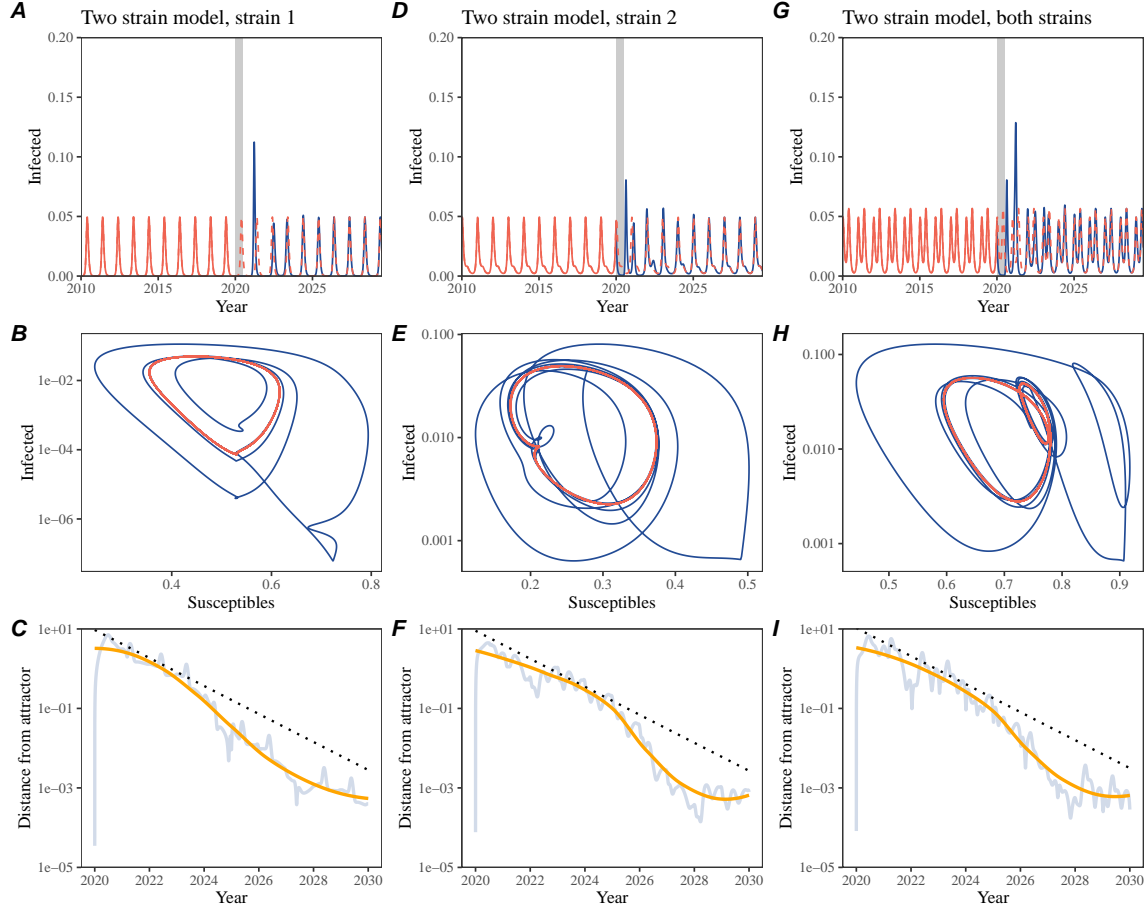


**Figure S3: Conceptual framework for measuring pathogen resilience following NPIs for a multi-strain system with seasonal forcing.** (A, D, G) Simulated epidemic trajectories using a multi-strain system with seasonal forcing (amplitude of 0.2). Red and blue solid lines represent epidemic dynamics before and after interventions are introduced, respectively. Red dashed lines represent counterfactual epidemic dynamics in the absence of interventions. Gray regions indicate the duration of interventions. (B, E, H) Phase plane representation of the corresponding model. Red and blue solid lines represent epidemic trajectories on an SI phase plane before and after interventions are introduced, respectively. (C, F, I) Changes in logged distance from attractor over time. Blue lines represent the logged distance from attractor. Orange lines represent the locally estimated scatterplot smoothing (LOESS) fits to the logged distance from attractor. Dotted lines are superimposed as a comparison to have the same slope as the intrinsic resilience of the seasonally unforced system.

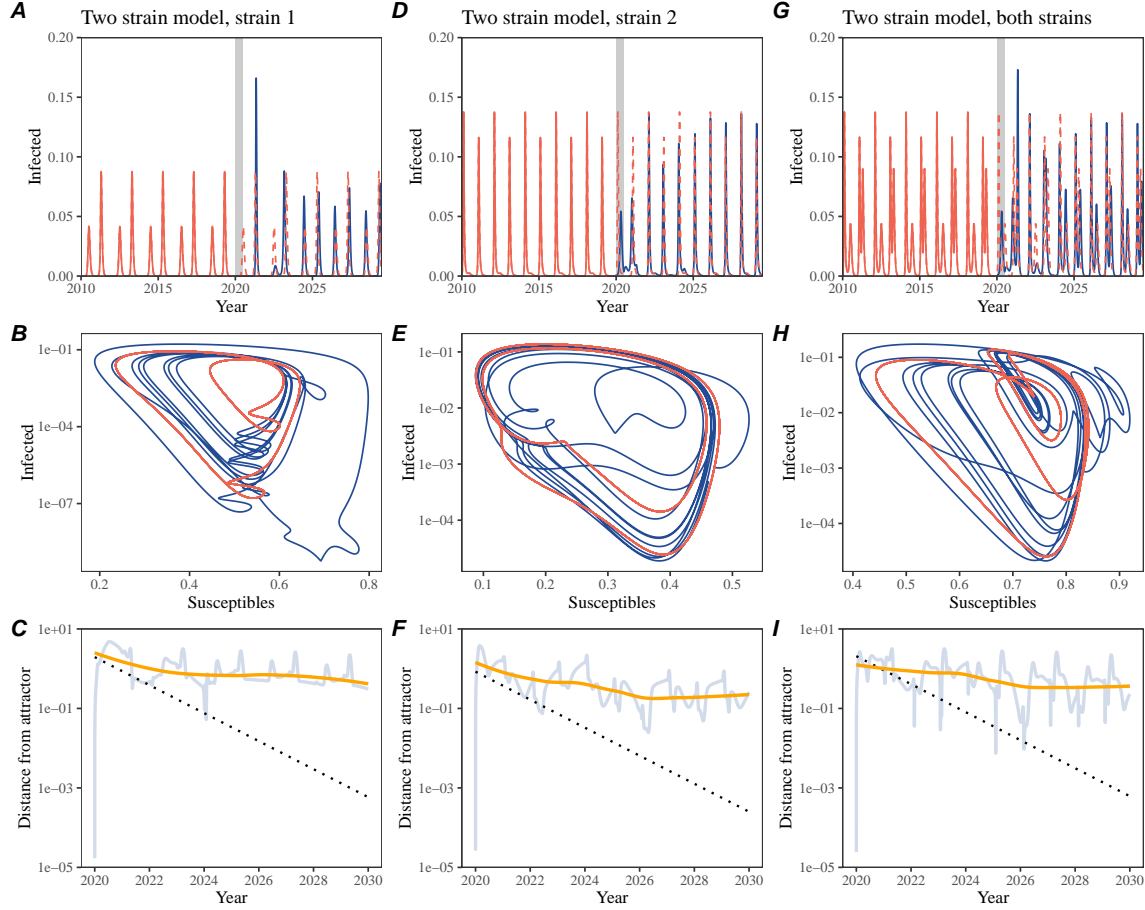


**Figure S4: Conceptual framework for measuring pathogen resilience following NPIs for a multi-strain system with strong seasonal forcing.** (A, D, G) Simulated epidemic trajectories using a multi-strain system with seasonal forcing (amplitude of 0.4). Red and blue solid lines represent epidemic dynamics before and after interventions are introduced, respectively. Red dashed lines represent counterfactual epidemic dynamics in the absence of interventions. Gray regions indicate the duration of interventions. (B, E, H) Phase plane representation of the corresponding model. Red and blue solid lines represent epidemic trajectories on an SI phase plane before and after interventions are introduced, respectively. (C, F, I) Changes in logged distance from attractor over time. Blue lines represent the logged distance from attractor. Orange lines represent the locally estimated scatterplot smoothing (LOESS) fits to the logged distance from attractor. Dotted lines are superimposed as a comparison to have the same slope as the intrinsic resilience of the seasonally unforced system.

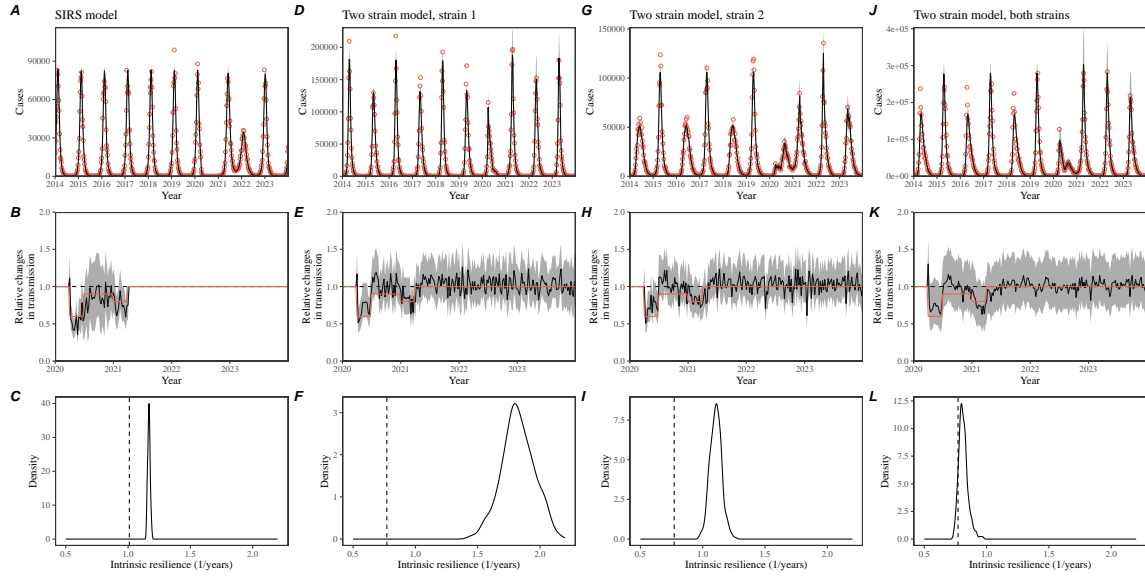


**Figure S5: Mechanistic model fits to simulated data and inferred intrinsic resilience.** (A, D, G, J) Simulated case time series from corresponding models (red) and SIRS model fits (black). (B, E, H, K) Assumed changes in transmission due to COVID-19 interventions (red) and estimated changes from the SIRS model (black). Solid lines and shaded regions represent fitted posterior median and 95% credible intervals. (C, F, I, L) True intrinsic resilience of the seasonally unforced system (vertical lines) and the posterior distribution of the inferred intrinsic resilience from the SIRS model (density plots).

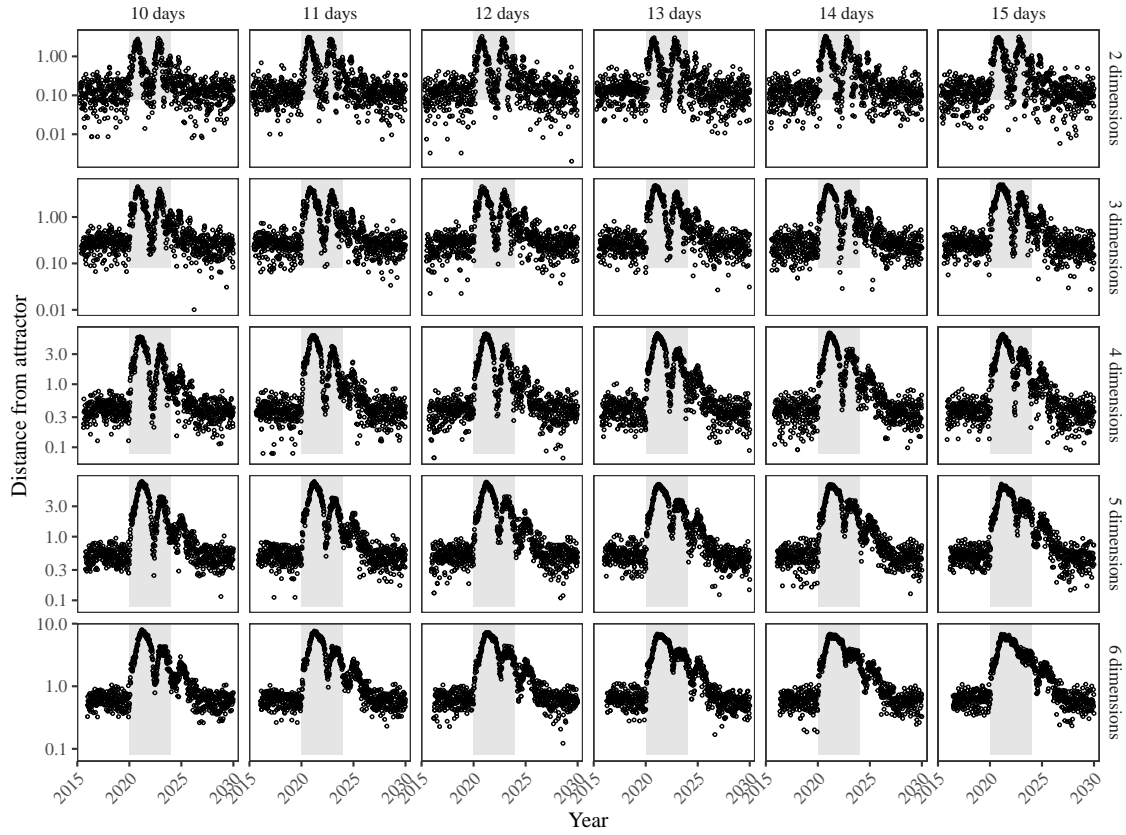


**Figure S6: Sensitivity of the distance from attractor to choices about embedding lags and dimensions.** Sensitivity analysis for the distance-from-attractor time series shown in Figure 3E in the main text by varying the embedding lag between 10–15 days and embedding dimensions between 2–6 dimensions.

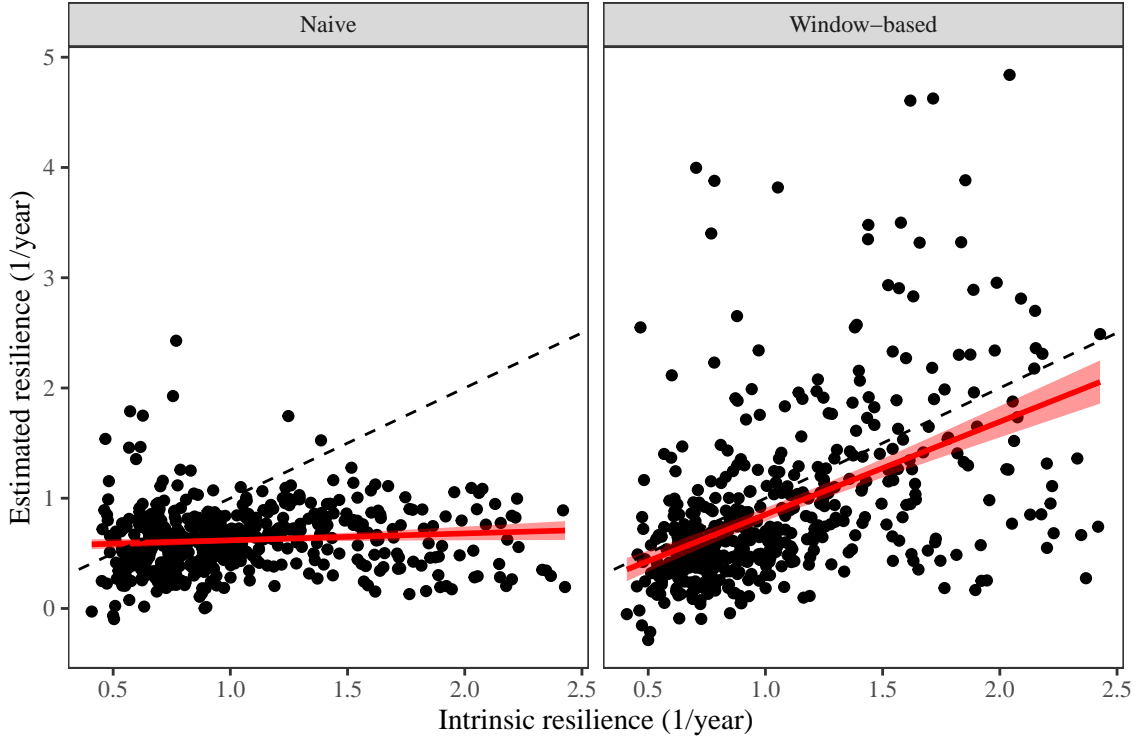


**Figure S7: Impact of fitting window selection on the estimation of empirical resilience.** We simulate 500 epidemics using stochastic SIRS model with randomly drawn parameters and randomly generated intervention impacts. For each simulation, we reconstruct the empirical attractor based on the approach outlined in Figure 3 and estimate the distance from attractor. The naive approach fits a linear regression on a log scale, starting from the maximum distance until the end of the time series. The window-based approach tries to select an appropriate window by smoothing the distance estimates and finding a time period when the smoothed time series crosses pre-determined threshold, relatively to the maximum distance; then, a linear regression is fitted by using the raw distance within this time period.

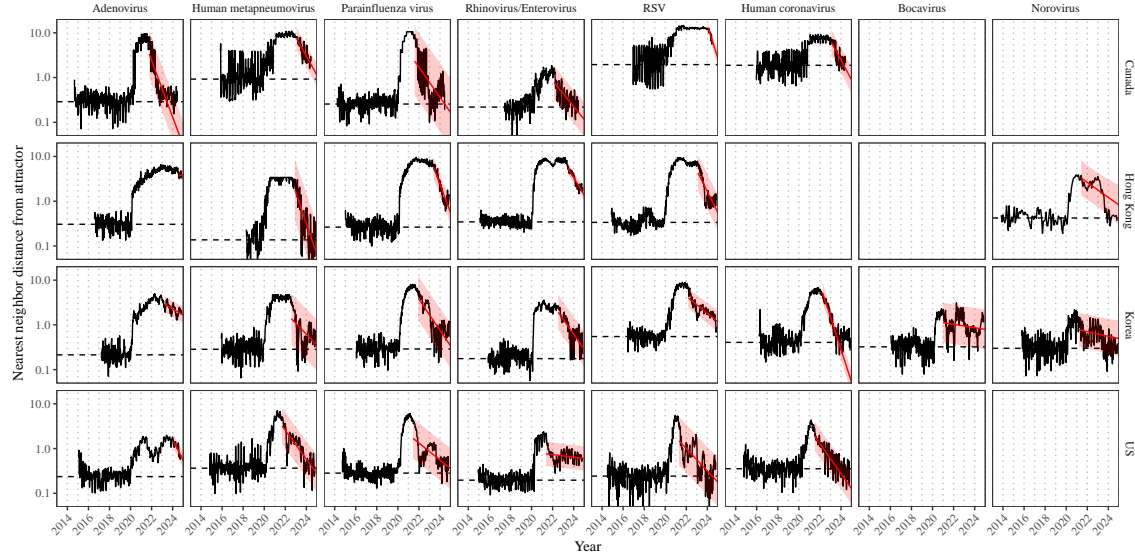


**Figure S8: Estimated time series of distance from attractor for each pathogen across Canada, Hong Kong, Korea, and the US.** Black lines represent the estimated distance from attractor. Red lines and shaded regions represent the linear regression fits and corresponding 95% confidence intervals. Dashed lines represent the average of the pre-pandemic nearest neighbor distances.

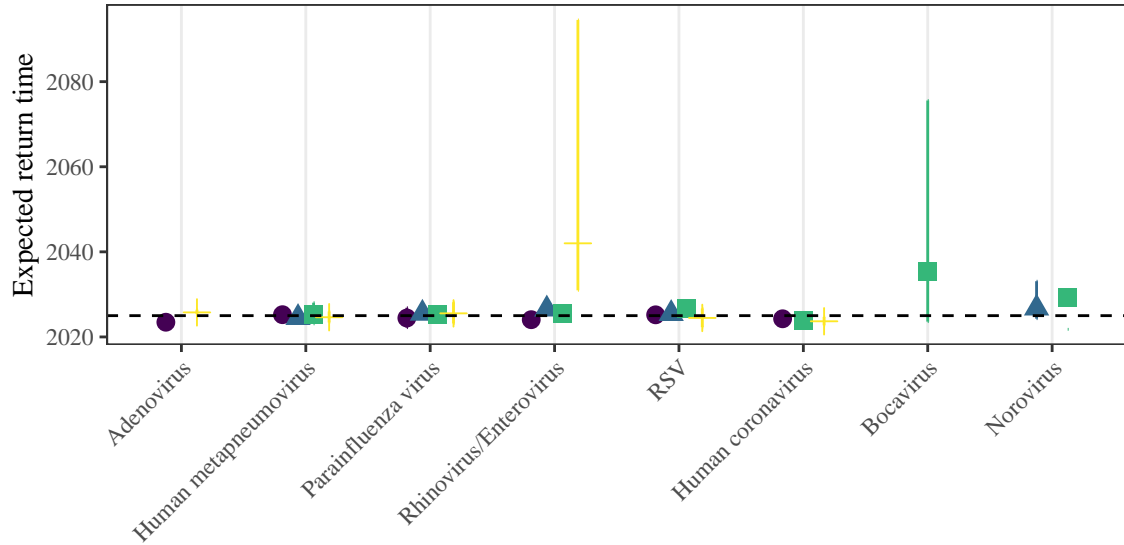
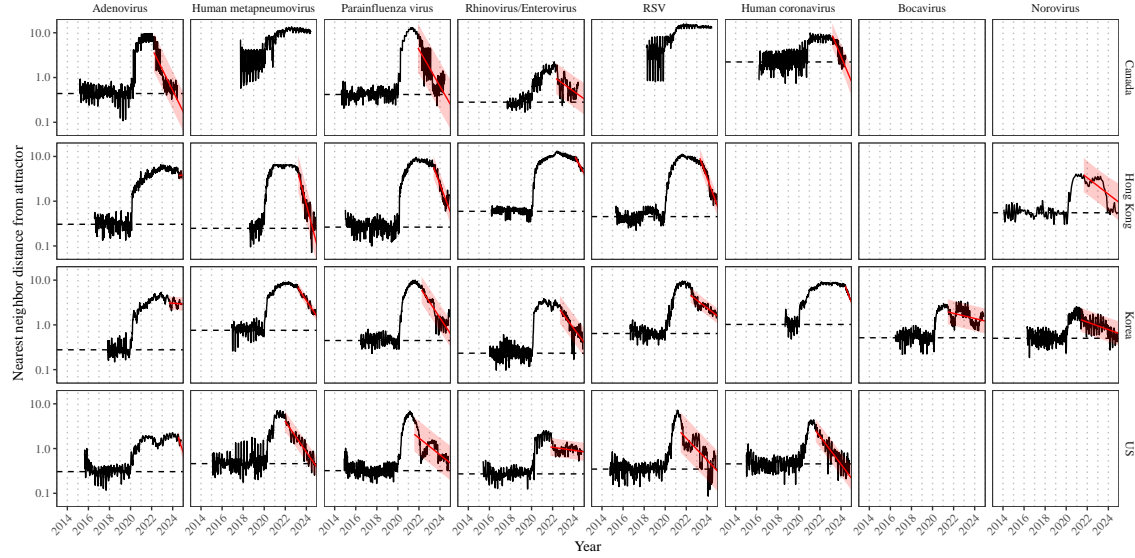


Figure S9: **Predicted timing of when each pathogen will return to their pre-pandemic cycles (zoomed out).** The dashed line in panel B indicates the end of 2024 (current observation time). Error bars represent 95% confidence intervals.



**Figure S10: Estimated time series of distance from attractor for each pathogen across Canada, Hong Kong, Korea, and the US using higher embedding dimensions.** Black lines represent the estimated distance from attractor. Red lines and shaded regions represent the linear regression fits and corresponding 95% confidence intervals. Dashed lines represent the average of the pre-pandemic nearest neighbor distances. A lower threshold is used for determining embedding dimensions with the false nearest neighbors approach, thereby yielding a higher embedding dimension.

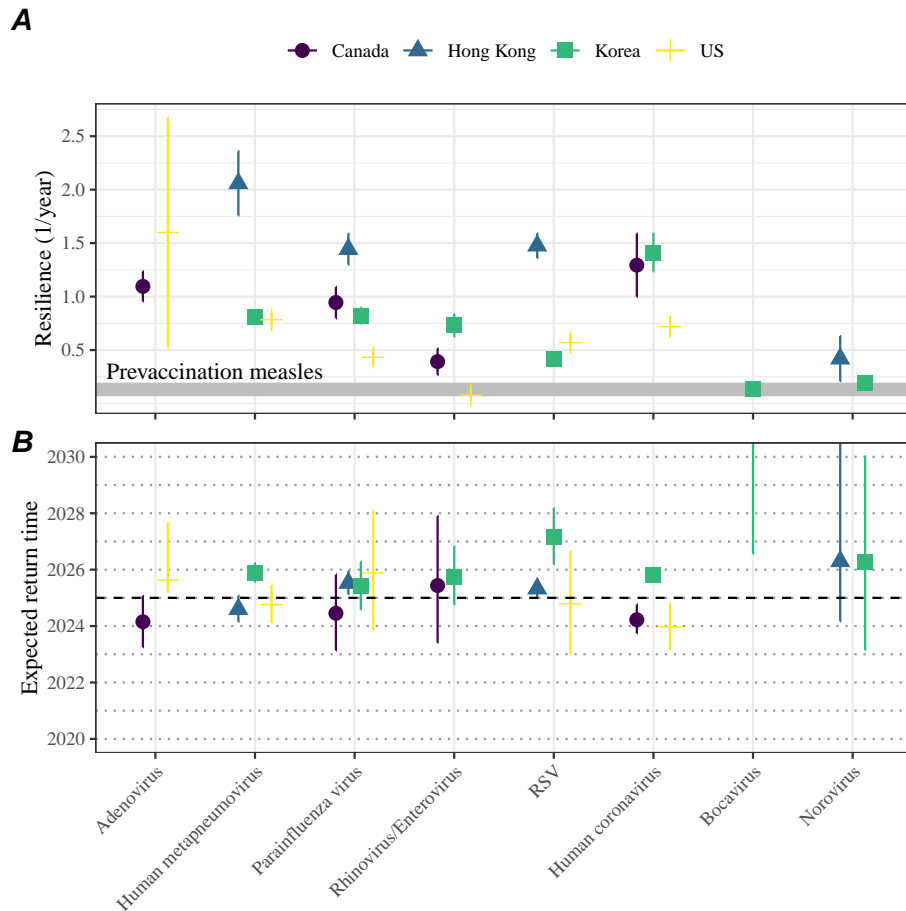


Figure S11: **Summary of resilience estimates using higher embedding dimensions.** (A) Estimated pathogen resilience. The gray horizontal line represents the intrinsic resilience of pre-vaccination measles dynamics. (B) Predicted timing of when each pathogen will return to their pre-pandemic cycles. The dashed line in panel B indicates the end of 2024 (current observation time). Error bars represent 95% confidence intervals. A lower threshold is used for determining embedding dimensions with the false nearest neighbors approach, thereby yielding a higher embedding dimension.

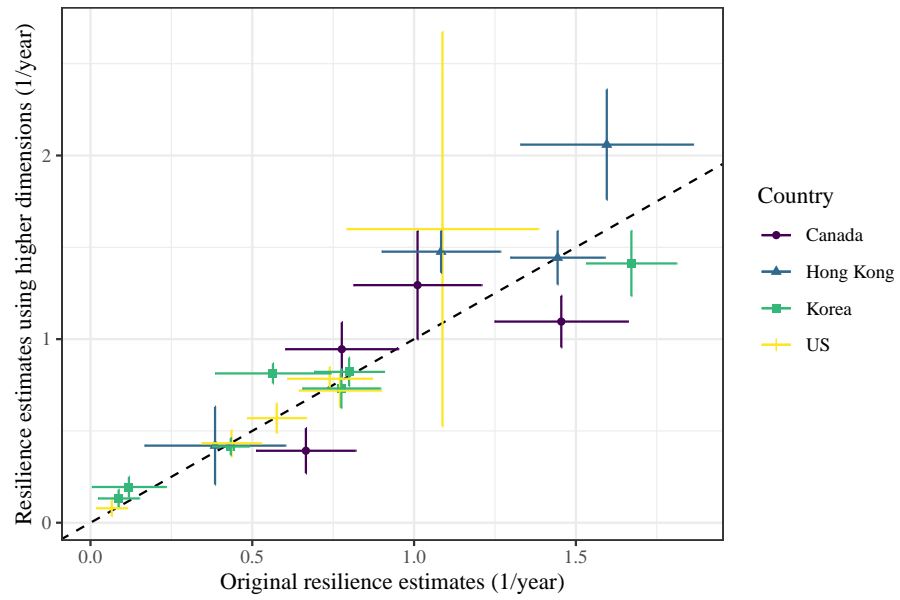


Figure S12: **Comparison of resilience estimates.** Each point represents a resilience estimate for a specific pathogen at a specific country. The x values represent the original resilience estimates presented in Figure 4. The y values represent the original resilience estimates presented in Supplementary Figure S11.

## 638 References

- 639 [1] Rachel E Baker, Sang Woo Park, Wenchang Yang, Gabriel A Vecchi, C Jessica E  
640 Metcalf, and Bryan T Grenfell. The impact of COVID-19 nonpharmaceutical  
641 interventions on the future dynamics of endemic infections. *Proceedings of the*  
642 *National Academy of Sciences*, 117(48):30547–30553, 2020.
- 643 [2] Gabriela B Gomez, Cedric Mahé, and Sandra S Chaves. Uncertain effects of the  
644 pandemic on respiratory viruses. *Science*, 372(6546):1043–1044, 2021.
- 645 [3] Mihaly Koltai, Fabienne Krauer, David Hodgson, Edwin van Leeuwen, Marina  
646 Treskova-Schwarzbach, Mark Jit, and Stefan Flasche. Determinants of RSV  
647 epidemiology following suppression through pandemic contact restrictions. *Epi-*  
648 *demics*, 40:100614, 2022.
- 649 [4] Sang Woo Park, Brooklyn Noble, Emily Howerton, Bjarke F Nielsen, Sarah  
650 Lentz, Lilliam Ambroggio, Samuel Dominguez, Kevin Messacar, and Bryan T  
651 Grenfell. Predicting the impact of non-pharmaceutical interventions against  
652 COVID-19 on *Mycoplasma pneumoniae* in the United States. *Epidemics*,  
653 49:100808, 2024.
- 654 [5] Eric J Chow, Timothy M Uyeki, and Helen Y Chu. The effects of the COVID-19  
655 pandemic on community respiratory virus activity. *Nature Reviews Microbiol-*  
656 *ogy*, 21(3):195–210, 2023.
- 657 [6] Stephen M Kissler, Christine Tedijanto, Edward Goldstein, Yonatan H Grad,  
658 and Marc Lipsitch. Projecting the transmission dynamics of SARS-CoV-2  
659 through the postpandemic period. *Science*, 368(6493):860–868, 2020.
- 660 [7] Rachel E Baker, Chadi M Saad-Roy, Sang Woo Park, Jeremy Farrar, C Jessica E  
661 Metcalf, and Bryan T Grenfell. Long-term benefits of nonpharmaceutical inter-  
662 ventions for endemic infections are shaped by respiratory pathogen dynamics.  
663 *Proceedings of the National Academy of Sciences*, 119(49):e2208895119, 2022.
- 664 [8] Edward A Bender, Ted J Case, and Michael E Gilpin. Perturbation experiments  
665 in community ecology: theory and practice. *Ecology*, 65(1):1–13, 1984.
- 666 [9] Anthony R Ives and Stephen R Carpenter. Stability and diversity of ecosystems.  
667 *science*, 317(5834):58–62, 2007.
- 668 [10] Marten Scheffer, Jordi Bascompte, William A Brock, Victor Brovkin, Stephen R  
669 Carpenter, Vasilis Dakos, Hermann Held, Egbert H Van Nes, Max Rietkerk,  
670 and George Sugihara. Early-warning signals for critical transitions. *Nature*,  
671 461(7260):53–59, 2009.
- 672 [11] Stuart L Pimm. The structure of food webs. *Theoretical population biology*,  
673 16(2):144–158, 1979.

- 674 [12] Michael G Neubert and Hal Caswell. Alternatives to resilience for measuring  
675 the responses of ecological systems to perturbations. *Ecology*, 78(3):653–665,  
676 1997.
- 677 [13] Lance H Gunderson. Ecological resilience—in theory and application. *Annual  
678 review of ecology and systematics*, 31(1):425–439, 2000.
- 679 [14] Vasilis Dakos and Sonia Kéfi. Ecological resilience: what to measure and how.  
680 *Environmental Research Letters*, 17(4):043003, 2022.
- 681 [15] Jeanne C Chambers, Craig R Allen, and Samuel A Cushman. Operationalizing  
682 ecological resilience concepts for managing species and ecosystems at risk.  
683 *Frontiers in Ecology and Evolution*, 7:241, 2019.
- 684 [16] Georgiy V Bobashev, Stephen P Ellner, Douglas W Nychka, and Bryan T  
685 Grenfell. Reconstructing susceptible and recruitment dynamics from measles  
686 epidemic data. *Mathematical Population Studies*, 8(1):1–29, 2000.
- 687 [17] Bärbel F Finkenstädt and Bryan T Grenfell. Time series modelling of childhood  
688 diseases: a dynamical systems approach. *Journal of the Royal Statistical Society  
689 Series C: Applied Statistics*, 49(2):187–205, 2000.
- 690 [18] Floris Takens. Detecting strange attractors in turbulence. In *Dynamical Sys-  
691 tems and Turbulence, Warwick 1980: proceedings of a symposium held at the  
692 University of Warwick 1979/80*, pages 366–381. Springer, 2006.
- 693 [19] Alan Hastings, Karen C Abbott, Kim Cuddington, Tessa Francis, Gabriel Gell-  
694 ner, Ying-Cheng Lai, Andrew Morozov, Sergei Petrovskii, Katherine Scran-  
695 ton, and Mary Lou Zeeman. Transient phenomena in ecology. *Science*,  
696 361(6406):eaat6412, 2018.
- 697 [20] Matthew B Kennel, Reggie Brown, and Henry DI Abarbanel. Determining  
698 embedding dimension for phase-space reconstruction using a geometrical con-  
699 struction. *Physical review A*, 45(6):3403, 1992.
- 700 [21] Eugene Tan, Shannon Algar, Débora Corrêa, Michael Small, Thomas Stemler,  
701 and David Walker. Selecting embedding delays: An overview of embedding  
702 techniques and a new method using persistent homology. *Chaos: An Interdis-  
703 ciplinary Journal of Nonlinear Science*, 33(3), 2023.
- 704 [22] Samit Bhattacharyya, Per H Gesteland, Kent Korgenski, Ottar N Bjørnstad,  
705 and Frederick R Adler. Cross-immunity between strains explains the dynamical  
706 pattern of paramyxoviruses. *Proceedings of the National Academy of Sciences*,  
707 112(43):13396–13400, 2015.

- 708 [23] Bryan T Grenfell, Ottar N Bjørnstad, and Bärbel F Finkenstädt. Dynamics of  
709 measles epidemics: scaling noise, determinism, and predictability with the TSIR  
710 model. *Ecological monographs*, 72(2):185–202, 2002.
- 711 [24] Virginia E Pitzer, Cécile Viboud, Vladimir J Alonso, Tanya Wilcox, C Jessica  
712 Metcalf, Claudia A Steiner, Amber K Haynes, and Bryan T Grenfell. Environmental  
713 drivers of the spatiotemporal dynamics of respiratory syncytial virus in  
714 the United States. *PLoS pathogens*, 11(1):e1004591, 2015.
- 715 [25] Katharine R Dean, Fabienne Krauer, Lars Walløe, Ole Christian Lingjærde, Bar-  
716 Barbara Bramanti, Nils Chr Stenseth, and Boris V Schmid. Human ectoparasites  
717 and the spread of plague in Europe during the Second Pandemic. *Proceedings  
718 of the National Academy of Sciences*, 115(6):1304–1309, 2018.
- 719 [26] Margarita Pons-Salort and Nicholas C Grassly. Serotype-specific immunity  
720 explains the incidence of diseases caused by human enteroviruses. *Science*,  
721 361(6404):800–803, 2018.
- 722 [27] Sarah Cobey and Edward B Baskerville. Limits to causal inference with state-  
723 space reconstruction for infectious disease. *PloS one*, 11(12):e0169050, 2016.
- 724 [28] Edward Goldstein, Sarah Cobey, Saki Takahashi, Joel C Miller, and Marc Lip-  
725 sitch. Predicting the epidemic sizes of influenza A/H1N1, A/H3N2, and B: a  
726 statistical method. *PLoS medicine*, 8(7):e1001051, 2011.
- 727 [29] Bob Carpenter, Andrew Gelman, Matthew D Hoffman, Daniel Lee, Ben  
728 Goodrich, Michael Betancourt, Marcus A Brubaker, Jiqiang Guo, Peter Li,  
729 and Allen Riddell. Stan: A probabilistic programming language. *Journal of  
730 statistical software*, 76, 2017.
- 731 [30] Stan Development Team. RStan: the R interface to Stan, 2024. R package  
732 version 2.32.6.